(1)

DEPARTMENT OF THE AIR FORCE

AIR UNIVERSITY

AIR FORCE INSTITUTE OF TECHNOLOGY

Wright-Patterson Air Force Base, Ohio

AFIT/GE/ENG/88D-51

SCATTERING CALCULATIONS FOR VARIOUS HAILSTONE MODELS USING THE EXTENDED BOUNDARY CONDITION METHOD

THESIS

Brian J. Stutz
Captain, USAF

AFIT/GE/ENG/88D-51

Approved for public release; distribution unlimited

AFIT/GE/ENG/88D-51

SCATTERING CALCULATIONS FOR VARIOUS HAILSTONE MODELS USING THE EXTENDED BOUNDARY CONDITION METHOD

THESIS

Presented to the Faculty of the School of Engineering
of the Air Force Institute of Technology
Air University
In Partial Fulfillment of the
Requirements for the Degree of
Master of Science in Electrical Engineering

Brian J. Stutz, B.S.
Captain, USAF

December 1988

Acknowledgments

I am indebted to several people who contributed in various ways in this learning experience. First, I would like to thank my advisor, Major Harry Barksdale, who got me interested in this project and guided me with great patience to its completion. Lt Col William Baker and Capt Randy Jost were my readers and I thank them for their support and expert advice. I would also like to thank Dr. Peter Barber at the Clarkson College of Technology for graciously providing his EBCM programs for this effort. Finally, I would like to thank my wife, Debbie, for her love, encouragement, and infinite patience.

Brian J. Stutz

Table of Contents

List of Figures

Abstract

The extended boundary condition method is applied to 3-D electromagnetic scattering problems involving hailstones modeled using Wang's three parameter hailstone representation. The theory of the extended boundary condition method is presented for axisymmetric, layered dielectric scatterers. Scattering calculations are graphically presented for various layered and nonlayered hailstone models for incident wavelengths of 1 and 10 cm. The layered hailstone models are constructed of ice surrounded by a layer of water and represent melting hailstones. Nonlayered hailstone models represent nonmelting hailstones and are composed entirely of ice. Hailstone size, shape, and structure were varied to determine their effect on scattering and absorption characteristics. The results indicate that resonance scattering is very sensitive to hailstone size, shape, and structure. Rayleigh scattering is sensitive to size and structure but much less dependent on hailstone shape.

SCATTERING CALCULATIONS FOR VARIOUS HAILSTONE MODELS USING THE EXTENDED BOUNDARY CONDITION METHOD

I. Introduction

Overview

This thesis determines the scattering characteristics of single, resonance sized, axisymmetric hailstone models using the Extended Boundary Condition Method (EBCM). This theoretical analysis is sponsored by the Air Force Wright Aeronautical Laboratories (AFWAL) at Wright-Patterson Air Force Base. This chapter presents general background material and a brief discussion of previous work on the problem. Information concerning the approach to solving the problem is also presented.

Background

Secure and reliable communications systems are key elements to any successful Air Force operation; success or failure of a mission depends on accurate communication of information. This information is increasingly being transmitted via millimeter wave satellite-to-earth communication links. Any attenuation, phase shift, or depolarization of the transmitted signals prior to receive

must be considered in the design of these systems. Atmospheric precipitation in the form of rain or hail can have a significant effect on millimeter wave propagation. Scattering by rain or hail also plays an important role in radar meteorology (14:1).

The effect of precipitation in the form of rain has been the subject of extensive research. Considerably less research has been directed toward the impact of hailstorms on millimeter wave propagation (14:1). Scattering effects of hailstorms can be determined experimentally or predicted theoretically. A theoretical investigation of hailstone scattering involves determining the individual electromagnetic scattering characteristics of the hailstones and modeling the distribution of the hailstones along the propagation path. This thesis will theoretically examine the individual hailstone scattering problem. In the microwave band hailstones are often resonance sized or on the order of a wavelength of the illuminating signal. A method to analyze the problem must be selected and applied to the selected hailstone models.

Scattering characteristics of axisymmetric objects can be theoretically determined using several techniques: integral equation formulations, moment methods, and finite element methods (6:227-323; 8:275-285; 9:202-214). One of the most accepted integral equation techniques is the Extended Boundary Condition Method (EBCM) introduced by P.

C. Waterman in 1965 (18:805-812). The EBCM will be used to handle the hailstone models considered in this thesis.

Problem

This thesis will use the EBCM to determine the scattering characteristics of single, resonance sized hailstone models. Wet and dry, axisymmetric models representing melting and nonmelting hailstones will be considered. Sample scattering characteristics of the hailstone models will be presented.

Summary of Current Knowledge

EBCM. P. C. Waterman proposed the EBCM for determining the radar cross section of smooth, perfectly conducting bodies illuminated by a known plane wave. The EBCM is a T-matrix method where the scattered field is ultimately determined through the use of a transformation matrix. Waterman found the EBCM to be well suited for determining scattering characteristics of smooth, resonance sized, axisymmetric shapes (18:811).

Several researchers followed up on Waterman's original work and found different applications for the method. The EBCM has been used to calculate scattering by multilayered and multiple, dielectric and conducting objects including spheroids, cones, and finite cylinders (3,5,11,15). The next chapter contains a review of significant contributions in the evolution of the EBCM.

Hailstone Models. Hailstones have been modeled as several different shapes to study their scattering affects. Among these are spherical models, oblate spheroidal models, and sphere-cone-spheroidal models. Layered and nonlayered models representing melting and nonmelting hailstones have been considered. The nonlayered models are composed entirely of ice while layered hailstones are modeled as ice surrounded by a film or layer of water (1,4,15). Pao K. Wang recently proposed a three parameter hailstone representation (16). This thesis will determine scattering characteristics of Wang's hailstone model. The next chapter looks at the various hailstone models in more detail.

Assumptions

One general assumption is necessary to determine the scattering characteristics of the hailstone models. For this thesis we assume the hailstone is illuminated by a known plane wave. This assumption is necessary so the problem can be analyzed using the EBCM.

Scope

This thesis is limited to axisymmetric, resonance sized hailstone models. Nonlayered hailstone models must be homogeneous. Although layered hailstone models will be examined, each layer must itself be homogeneous. The hailstone models considered are composed of pure ice and water at zero degrees Celsius.

Approach

The major tasks in this thesis are as follows:

(1) Modify an existing EBCM program to determine layered and nonlayered hailstone model scattering characteristics.

(2) Test the program by duplicating previously published results.

(3) Using the program, determine the scattering characteristics of the Wang hailstone models.

Materials and Equipment

An EBCM computer program to be modified for the hailstone models is required for this analysis. Dr. Peter Barber at the Clarkson College of Technology graciously provided his EBCM programs. AFIT's CSC and ICC computer systems are required to compile and execute the EBCM code.

Sequence of Presentation

Chapter II will review the literature pertinent to this thesis. Chapter III will discuss the EBCM theory for layered dielectric scatterers and discuss Wang's hailstone model. Chapter IV will present the scattering results for a sample of hailstone models. Chapter V will summarize the effort and make recommendations for future research efforts.

II. Review of Literature

Introduction

Electromagnetic scattering characteristics of inhomogeneous, axisymmetric objects can be theoretically determined using several techniques: integral equation formulations, moment methods, and finite element methods (6:227-323; 8:275-285; 9:202-214). Each technique has particular advantages and limitations with respect to scatter size and shape. One of the most accepted integral equation techniques for resonance sized, axisymmetric scatterers is the Extended Boundary Condition Method (EBCM) introduced by P. C. Waterman in 1965 (18:805-812). This literature review examines significant contributions in the evolution of the EBCM. Various hailstone models which have been studied are also reviewed.

Background

Electromagnetic scattering problems involve an incident wave and a scattering object. The incident wave impinges upon the object and sets up currents in and on the object. These induced currents create an electromagnetic field which radiates in all directions. The nature of the incident wave and the geometry and composition of the scattering object determine the characteristics of the scattered electromagnetic field. Maxwell's equations and appropriate

boundary conditions can be used to relate the induced current and scattered field to the incident wave and scattering body (7:52).

Scattering Regimes. Electromagnetic wave scattering problems are characterized by the relationship between incident wavelength and scatterer size. The spectrum of scattering problems is divided into three regimes: the Rayleigh region where incident wavelength is much larger than the body size, the resonance region where incident wavelength is on the order of body size and the optics region where incident wavelength is much smaller than the body size (7:53). In general, an analytic technique for solving scattering problems is applicable to one of the three regimes. The EBCM is most applicable to scattering problems in the resonance region (3:2864).

Resonance Region Scattering. Figure 1 shows a typical scattering problem. The scatterer, S, is illuminated by a plane wave, $\vec{E}_i$ and $\vec{H}_i$, traveling in direction $\hat{k}$. $\vec{E}_s$ and $\vec{H}_s$ are the resulting scattered fields. For a resonance sized scatterer, the phase of the incident field changes over the length of the scatterer. Analyzing a resonance region scattering problem requires considering the affect of each part of the scatterer to every other part (7:57). Rayleigh and optics approximations can not be used since the complete wave nature of the incident field must be considered in the scattering problem (3:2864).

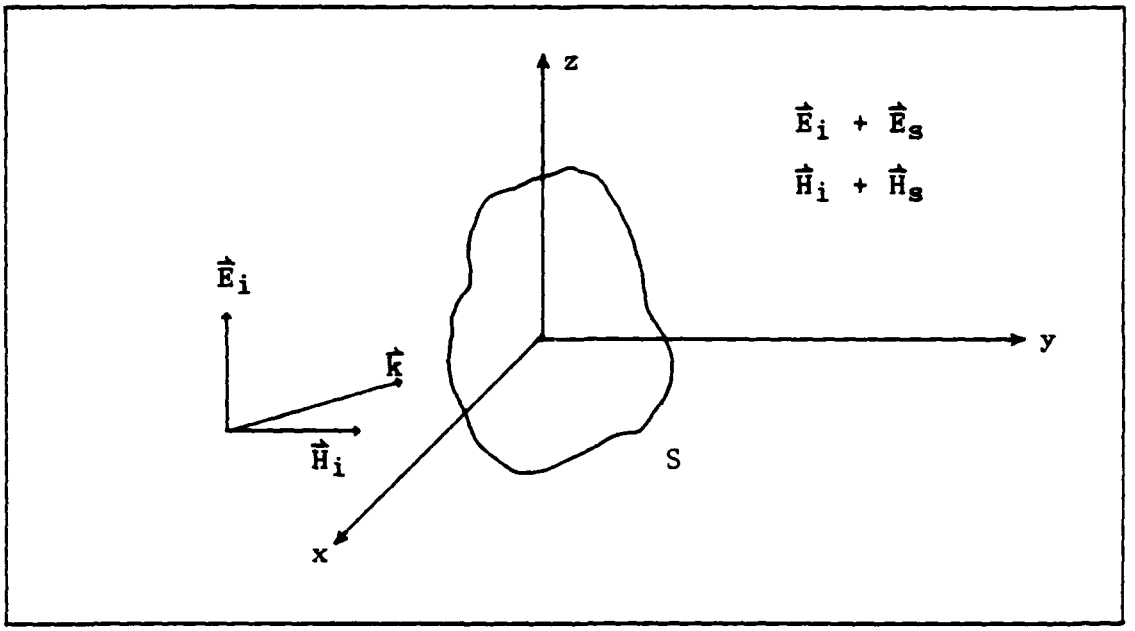

Figure 1. Electromagnetic Scattering

Origin of the EBCM

P. C. Waterman proposed a new method, the EBCM, for determining the radar cross section and other scattering quantities for smooth, perfectly conducting bodies illuminated by an incident plane wave (18:805). In the EBCM, known and unknown fields are expanded into infinite series of spherical vector wave functions. Numerically, the infinite series expansions are truncated at some value determined by convergence testing. The unknown expansion coefficients are solved for in terms of the known coefficients via a transformation or T-matrix. Waterman implemented the method on a computer and determined the radar cross section (RCS) of a sphere-cone-sphere. He found

the EBCM to be well suited for handling smooth axisymmetric shapes. Computation of surface current, scattered field, and differential scattering cross section were also accomplished with little additional computer time (18:811). Waterman noted no deterioration of results as frequency increased with respect to scatterer size and that no numerical difficulties were observed for resonance sized objects (18:811). Although resonance was not a problem, Waterman observed "poor numerical convergence of the truncation procedure" when the method was applied to elongated shapes with a length-to-width greater than two (18:811).

In a later article, Waterman expanded his method to compute the RCS of two types of conducting objects with edges: cone-spheres and right cylinders. The theoretical results from the cone-sphere and cylinder compared well with experimental measurements. Perfectly conducting, prolate and oblate spheroids were also examined and compared to geometrical-optics solutions. Agreement of the two methods was not good for resonance sized spheroids. This was expected because geometrical-optics methods are generally not applicable to problems in the resonance region. The two methods compared well for larger spheroids (19:825-839).

Multilayered and Dielectric Scatterers

Waterman's work had been limited to homogeneous perfectly conducting bodies. Peterson and Strom showed

Waterman's method could be extended to apply to multilayered and multiple, dielectric scatterers. Peterson and Strom's work was mostly theoretical but some numerical computation was accomplished. Resonance sized dielectric spheres were examined. Also, the RCS of a perfectly conducting sphere embedded in a concentric dielectric sphere was computed. The EBCM produced exact solutions for scattering by spheres (11:2670-2684).

Bringi and Seliga followed Peterson and Strom's work on multilayered, axisymmetric scatterers (5:575-580). Unlike Peterson and Strom who used the Poincare-Huygens principle, Bringi and Seliga derived the EBCM equations for multilayered scatterers using the equivalence principle. Bringi and Seliga used the method to compute scattering characteristics of dielectric spheres or conductors embedded in a spherical dielectric shell. The results compared well to extended Mie theory calculations. Bringi and Seliga thought the method would be well suited to examine the problem of scattering by melting hailstones (5:580).

Independent of Peterson and Strom, Barber and Yeh solved axisymmetric, dielectric scattering problems using the EBCM (3:2864-2872). The scattering objects considered were resonance sized, dielectric spheres, prolate and oblate spheroids, and finite cylinders (3:2864-2872). In a later work, Barber proposed a method for extending the region of applicability of the EBCM for highly elongated or high loss

objects. Barber's proposal consisted of making a set of calculations for a series of reduced dielectric constants where good results were found. The desired characteristics could then be extrapolated from a resulting curve for the dielectric constant of interest (2:380).

Other independent work on Waterman's method was conducted by Warner and Hizal (17:921-930). Warner and Hizal were interested in applying the EBCM to determine attenuation and depolarization effects of rain on microwave transmissions (17:921). Single raindrops were modeled as homogeneous, dielectric oblate spheroids and results from the EBCM compared well with previously published work. Warner and Hizal concluded that Waterman's method could be applied to hailstone models as well (17:928).

Hailstone Models

Hailstones of various size have been modeled as axisymmetric, geometrical shapes. Among these are spherical models, oblate spheroidal models, and sphere-cone-spheroidal models. Pao K. Wang recently proposed a three parameter hailstone representation. His model is different than previous models in that size and shape distributions can be described more quantitatively (16:1062). Figure 2 shows the general shapes of different hailstone models.

Spherical Hailstone Model. Battan, Browning, and Herman modeled hailstones as spheres and determined scattering characteristics using the extended Mie theory.

Wet and dry hailstone models were considered. The wet model, representing a melting hailstone, was a sphere of ice surrounded by a slightly larger diameter shell of water (4). Battan Browning, and Herman were the first to examine the hailstone scattering problem and their results provided a basis for comparison of future work.

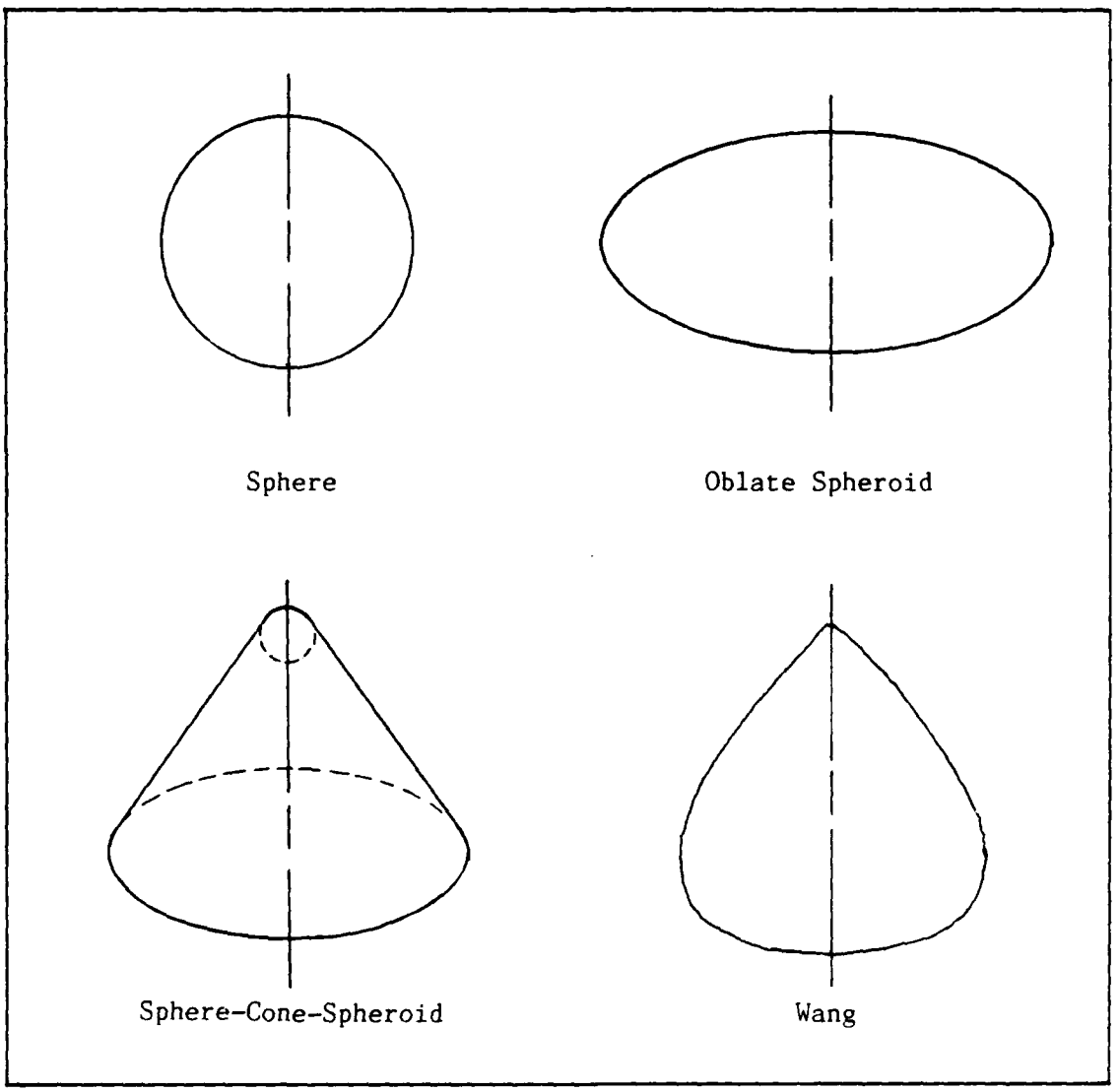

Figure 2. Hailstone Models

Oblate Spheroidal Hailstone Model. The extended Mie theory used by Battan, Browning, and Herman can be used to solve problems involving concentric spheres. Other methods must be used for aspherical shapes. Wang and Barber used the EBCM to determine scattering characteristics of oblate spheroidal models of hailstones. They compared layered oblate spheroidal models of varying size and axial ratio with corresponding equivolume spheres. Although absorption behavior was similar, the oblate spheroidal models generally scattered more incident radiation than an equivolume sphere. For axial incidence, backscattering increased significantly with increased axial ratio. Wang and Barber concluded that careful modeling of layered physical objects is important to obtain accurate theoretical calculations (15:1190-1197).

Sphere-Cone-Spheroidal Hailstone Model. Aydin and Seliga modeled hailstones as sphere-cone-spheres and sphere-cone-oblate spheroids. They used the EBCM for their backscatter analysis and also examined the oblate spheroid hailstone model used by Wang and Barber. Layered and homogeneous models representing melting and nonmelting hailstones were considered at 3 GHz. Effects due to various water coating thicknesses were examined (1:58-66). The scattering characteristics of the sphere-cone-spheroidal hailstone models were compared to equivolume spherical models. Backscattering characteristics varied with

hailstone size, shape and composition.

Wang's Hailstone Representation. Pao K. Wang's three parameter hailstone representation was used to analyze the size and shape distribution of a sample of 679 hailstones. The hailstones were collected during a hailstorm in Colorado. The analysis revealed simple relations between the number concentrations of hailstones and each of the three hailstone parameters. This study was concerned with size and shape characteristics of hailstones (16:1062-1070). The Wang hailstone model will be discussed in more detail in the next chapter. Theoretical scattering characteristics of Wang's hailstone model have not been determined.

Summary

Several applications and their contribution to the evolution of the EBCM have been reviewed. The method has been used to determine scattering and absorption characteristics of resonance sized, perfectly conducting and dielectric, axisymmetric bodies. Multilayered bodies and objects larger than incident wavelength have been examined using the EBCM. Scattering characteristics of spherical and oblate spheroidal models of wet and dry hailstones have been determined. Scattering characterization of Wang's hailstone representation have not been reported.

This chapter presented a review of literature pertaining to the EBCM and hailstone models. The next chapter presents the theory of the EBCM for layered,

axisymmetric, dielectric scatterers. Size and shape characteristics of Wang's hailstone model will also be discussed in the next chapter.

III. Theory

Overview

This chapter summarizes the theory of the EBCM for a two-layered, axisymmetric, dielectric scatterer. The notation and most equations in this summary are taken from the EBCM theory presented by Wang and Barber (15). Consult Peterson and Strom (11) for a detailed discussion of the method for multilayered scatterers. This chapter also discusses the size and shape characteristics of hailstones using Wang's three parameter hailstone representation.

The Scattering Problem

Figure 3 is a model of the problem of electromagnetic scattering by a two-layered object. For this problem there

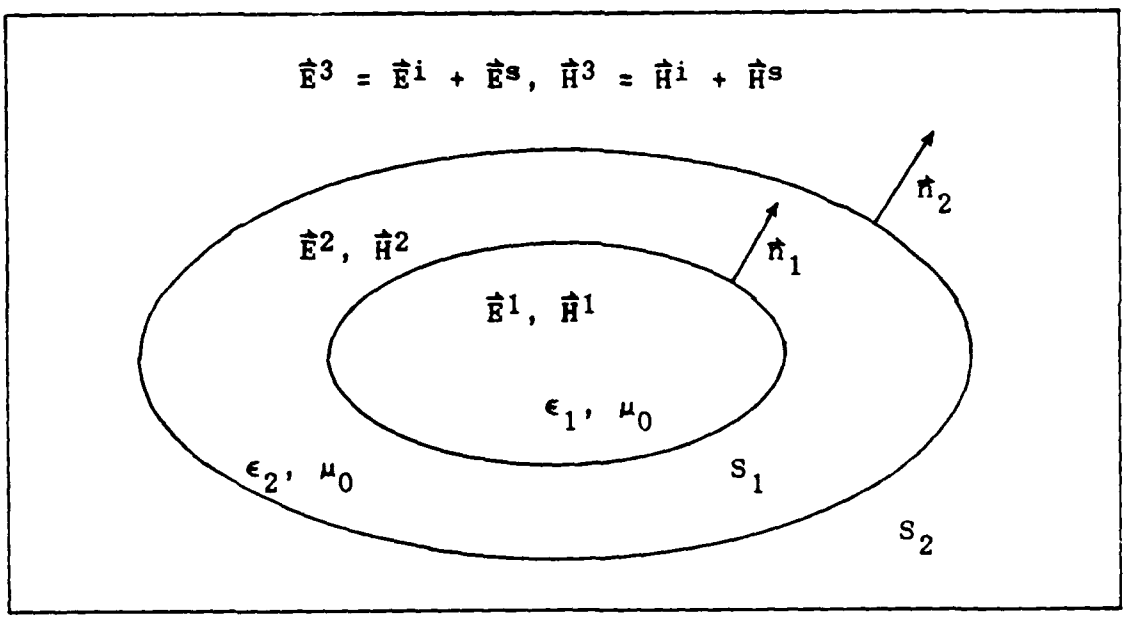

Figure 3. Layered Scattering Problem

are three regions separated by object surfaces S_1 and S_2. $\hat{E}^1$, $\hat{H}^1$; $\hat{E}^2$, $\hat{H}^2$; and $\hat{E}^3$, $\hat{H}^3$ are the fields in regions 1, 2 and 3 respectively. $\hat{E}^i$, $\hat{H}^i$ is the known incident field and $\hat{E}^s$, $\hat{H}^s$ is the unknown scattered field. As shown in the figure, the total field in region 3, ($\hat{E}^3$, $\hat{H}^3$), is the sum of the incident and scattered fields. Each of the three regions of the problem has the permeability of free space, μ_0, and a complex permittivity, ϵ_i, where i = 1, 2, or 3. Each region also has an associated complex wave number k_i.

$$k_i = (2\pi/\lambda_0)(\epsilon_i/\epsilon_0)^{1/2} \qquad (1)$$

where λ_0 is the free-space wavelength. Outward directed normal unit vectors to surfaces S_1 and S_2 are shown as $\hat{n}_1$ and $\hat{n}_2$.

Our goal is to determine the scattering characteristics of the object. To achieve this goal we will solve for the scattered field in terms of the known incident field and scatterer properties. The fields will be expanded using spherical vector wave functions. The expansion coefficients of the incident field are known and all other field expansion coefficients are unknown. The solution ultimately relates the scattered field expansion coefficients to the known incident field expansion coefficients via a transformation or T-matrix. To find our solution using the

EBCM, we will make the following assumptions: the object is axisymmetric and the complex permittivity within each region is constant throughout that region. We also assume an $\exp(-j\omega t)$ time variation.

Theoretical Development

The equivalence theorem permits us to reduce the original problem of Figure 3 to the three subproblems shown in Figure 4. For each subproblem, the surface currents $\vec{J}$ and $\vec{M}$ produce the actual field in the region of interest and a null field elsewhere. The plus (+) and minus (-) subscripts indicate external and internal field quantities, respectively, evaluated at the surface.

First, we examine the subproblem shown in Figure 4a. The scattered field external to S_2 is due to surface currents $\vec{J}_+^2$ and $\vec{M}_+^2$ and can be found using vector potentials $\vec{A}$ and $\vec{F}$.

$$\vec{E}^s = -\nabla\times\vec{F} - \frac{1}{j\omega\epsilon_0}(\nabla\times\nabla\times\vec{A}) \tag{2a}$$

$$\vec{H}^s = \nabla\times\vec{A} - \frac{1}{j\omega\mu_0}(\nabla\times\nabla\times\vec{F}) \tag{2b}$$

where

$$\vec{A} = \frac{1}{4\pi}\int_{S_2}\frac{\vec{J}_+^2\exp(jk_3|\vec{r}-\vec{r}'|)}{|\vec{r}-\vec{r}'|}\,ds' \tag{3a}$$

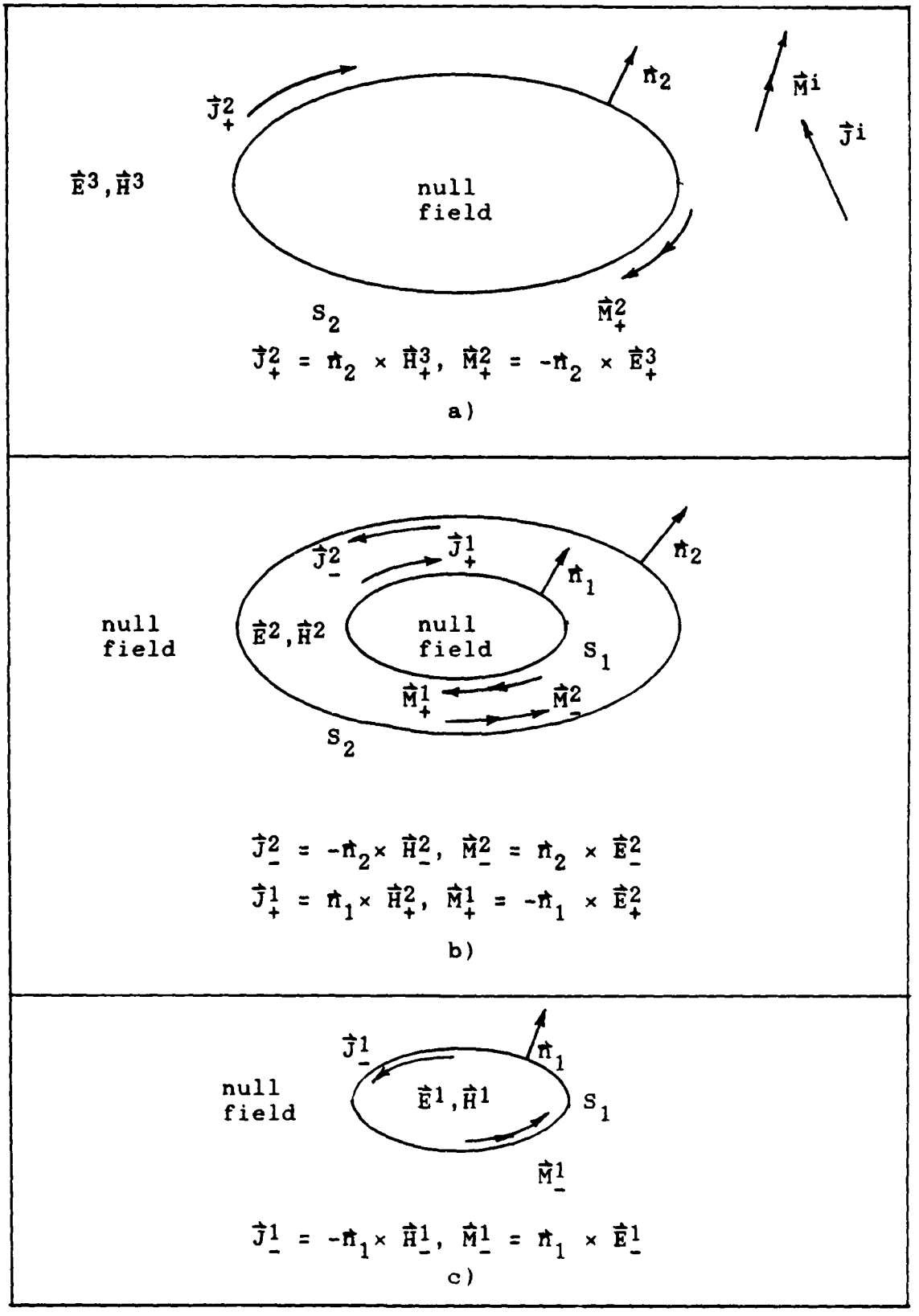

Figure 4. Equivalence Theorem Subproblems

$$\vec{F} = \frac{1}{4\pi} \int_{S_2} \frac{\vec{M}_+^2 \exp(jk_3|\vec{r} - \vec{r}'|)}{|\vec{r} - \vec{r}'|} \, ds' \tag{3b}$$

and

$$\vec{J}_+^2 = \hat{n}_2 \times \vec{H}_+^3 \tag{4a}$$

$$\vec{M}_+^2 = - \hat{n}_2 \times \vec{E}_+^3 \tag{4b}$$

The position vectors $\vec{r}$ and $\vec{r}'$ in Equation 2 indicate observation and source points respectively.

The total field external to S_2 in Figure 2a is the sum of the incident and scattered fields. So, for $\vec{r}$ outside S_2 we have

$$\vec{E}^3(\vec{r}) = \vec{E}^i(\vec{r}) + \vec{E}^s(\vec{r}) \tag{5a}$$

A null field exists within S_2, so for $\vec{r}$ inside S_2 we have

$$0 = \vec{E}^i(\vec{r}) + \vec{E}^s(\vec{r}) \tag{5b}$$

Substituting Equations 2 through 4 into Equation 5 yields the following set of integral equations

$$\hat{\mathbf{E}}^i(\hat{\mathbf{r}}) + \nabla \times \int_{S_2} (\hat{\mathbf{n}}_2 \times \hat{\mathbf{E}}^3_+) g(k_3 R) ds'$$

$$- \nabla \times \nabla \times \int_{S_2} \frac{1}{j\omega\epsilon_3} (\hat{\mathbf{n}}_2 \times \hat{\mathbf{H}}^3_+) g(k_3 R) ds'$$

$$= \begin{cases} \hat{\mathbf{E}}^3(\hat{\mathbf{r}}) & ; \ \hat{\mathbf{r}} \text{ outside } S_2 \quad (6a) \\ 0 & ; \ \hat{\mathbf{r}} \text{ inside } S_2 \quad (6b) \end{cases}$$

where $g(k_i R)$ is the free-space Green's function for region i

$$g(k_i R) = \frac{\exp(jk_i R)}{4\pi R} \quad (7a)$$

$$R = |\hat{\mathbf{r}} - \hat{\mathbf{r}}'| \quad (7b)$$

Now we look at the subproblem shown in Figure 4b. In this subproblem, the surface currents produce a field in the region between surfaces S_1 and S_2 and a null field outside S_2 and inside S_1. The following set of integral equations results from analysis of this subproblem

$$\nabla \times \int_{S_2} (-\hat{\mathbf{n}}_2 \times \hat{\mathbf{E}}^2_-) g(k_2 R) ds' - \nabla \times \nabla \times \int_{S_2} \frac{1}{j\omega\epsilon_2} (-\hat{\mathbf{n}}_2 \times \hat{\mathbf{H}}^2_-) g(k_2 R) ds'$$

$$+ \nabla \times \int_{S_1} (\hat{\mathbf{n}}_1 \times \hat{\mathbf{E}}^2_+) g(k_2 R) ds' - \nabla \times \nabla \times \int_{S_1} \frac{1}{j\omega\epsilon_2} (\hat{\mathbf{n}}_1 \times \hat{\mathbf{H}}^2_+) g(k_2 R) ds'$$

$$= \begin{cases} \hat{\mathbf{E}}^2(\hat{\mathbf{r}}) & ; \ \hat{\mathbf{r}} \text{ between } S_1 \text{ and } S_2 \quad (8a) \\ 0 & ; \ \hat{\mathbf{r}} \text{ outside } S_2 \text{ and inside } S_1 \quad (8b) \end{cases}$$

We now have integral equation representations of the subproblems of Figure 4a and 4b. Similar equations can be

written for the subproblem of Figure 4c but are not necessary in this analysis. Boundary conditions exist at object surfaces S_1 and S_2 enabling us to relate Equations 7 and 8 and ultimately solve the scattering problem. At object surfaces S_1 and S_2 the tangential fields must be continuous. Thus, we have the following boundary conditions:

$$\hat{n}_2 \times \vec{E}^3_+ = \hat{n}_2 \times \vec{E}^2_- \tag{9a}$$

$$\hat{n}_2 \times \vec{H}^3_+ = \hat{n}_2 \times \vec{H}^2_- \tag{9b}$$

$$\hat{n}_1 \times \vec{E}^2_+ = \hat{n}_1 \times \vec{E}^1_- \tag{9c}$$

$$\hat{n}_1 \times \vec{H}^2_+ = \hat{n}_1 \times \vec{H}^1_- \tag{9d}$$

Substituting Equations 9a and 9b into Equation 6 and Equations 9b and 9c into Equation 8 we have

$$\vec{E}^i(\vec{r}) + \nabla \times \int_{S_2} (\hat{n}_2 \times \vec{E}^2_-) \cdot \overline{\overline{G}}(k_3 R) ds' - \nabla \times \nabla \times \int_{S_2} \frac{1}{j\omega\epsilon_3} (\hat{n}_2 \times \vec{H}^2_-) \cdot \overline{\overline{G}}(k_3 R) ds' = \begin{cases} \vec{E}^3(\vec{r}) & ; \ \vec{r} \text{ outside } S_2 \quad (10a) \\ 0 & ; \ \vec{r} \text{ inside } S_2 \quad (10b) \end{cases}$$

$$\nabla \times \int_{S_2} (-\hat{n}_2 \times \vec{E}_-^2) \cdot \overline{G}(k_2 R) ds' - \nabla \times \nabla \times \int_{S_2} \frac{1}{j\omega\epsilon_2} (-\hat{n}_2 \times \vec{H}_-^2) \cdot \overline{G}(k_2 R) ds'$$

$$+ \nabla \times \int_{S_1} (\hat{n}_1 \times \vec{E}_-^1) \cdot \overline{G}(k_2 R) ds' - \nabla \times \nabla \times \int_{S_1} \frac{1}{j\omega\epsilon_2} (\hat{n}_1 \times \vec{H}_-^1) \cdot \overline{G}(k_2 R) ds'$$

$$= \begin{cases} \vec{E}^2(\vec{r}) & ; \ \vec{r} \text{ between } S_1 \text{ and } S_2 \quad (11a) \\ 0 & ; \ \vec{r} \text{ outside } S_2 \text{ and inside } S_1 \quad (11b) \end{cases}$$

The free-space Green's dyadic, $\overline{G}(k_i R)$, was used in Equations 10 and 11. This is necessary to numerically solve the integral equations for the scattered field. The dyadic Green's function and the fields in Equations 10 and 11 will be expanded in spherical vector wave functions $\vec{M}$ and $\vec{N}$ (13:415).

$$\vec{M}^p_{\sigma mn}(k\vec{r}) = \nabla \times \vec{r} \begin{matrix} \cos(m\phi) \\ \sin(m\phi) \end{matrix} P_n(\cos\theta) z_n^p(kr) \quad (12a)$$

$$\vec{N}^p_{\sigma mn}(\vec{r}) = \frac{1}{k} \nabla \times \vec{M}^p_{\sigma mn}(\vec{r}) \quad (12b)$$

where $P_n^m(\cos\theta)$ is an associated Legendre function, σ is even or odd, and $z_n^p(kr)$ is an appropriate spherical Bessel function.

$$z_n^p(kr) = \begin{cases} j_n(kr) & ; \ p = 1 \\ j_n(kr) + jn_n(kr) & ; \ p = 3 \end{cases} \quad (13)$$

The dyadic Green's function expansion is given as

$$\overline{G}(kR) = \frac{jk}{\pi} \sum_{\nu} D_\nu [\vec{M}^3_\nu(k\vec{r}_>) \vec{M}^1_\nu(k\vec{r}_<) + \vec{N}^3_\nu(k\vec{r}_>) \vec{N}^1_\nu(k\vec{r}_<)] \quad (14)$$

where $\hat{r}_>$ is the greater of $\hat{r}$ or $\hat{r}'$, $\hat{r}_<$ is the lesser of $\hat{r}$ or $\hat{r}'$, and D_ν is a normalization constant (10:1781). The summation over ν is a combined summation:

$$\sum_\nu = \sum_{\substack{\sigma=e \\ o}} \sum_{n=1}^{\infty} \sum_{m=0}^{n} \tag{15a}$$

$$D_\nu = \frac{\epsilon_m (2n+1)(n-m)!}{4n(n+1)(n+m)!} \tag{15b}$$

$$\epsilon_m = \begin{cases} 1 \; ; \; m = 0 \\ 2 \; ; \; m > 0 \end{cases} \tag{15c}$$

The fields in Equations 10 and 11 are also expanded in terms of $\hat{M}$ and $\hat{N}$.

$$\hat{E}^i(\hat{r}) = \sum_\nu D_\nu [a_\nu \hat{M}^1_\nu(k_3\hat{r}) + b_\nu \hat{N}^1_\nu(k_3\hat{r})] \tag{16a}$$

$$\hat{E}^s(\hat{r}) = \sum_\nu 4D_\nu [f_\nu \hat{M}^3_\nu(k_3\hat{r}) + g_\nu \hat{N}^3_\nu(k_3\hat{r})] \tag{16b}$$

$$\hat{E}^2(\hat{r}) = \sum_\nu D_\nu [\tau_\nu \hat{M}^1_\nu(k_2\hat{r}) + \delta_\nu \hat{N}^1_\nu(k_2\hat{r}) + \alpha_\nu \hat{M}^3_\nu(k_2\hat{r}) + \beta_\nu \hat{N}^3_\nu(k_2\hat{r})] \tag{16c}$$

$$\hat{E}^1(\hat{r}) = \sum_\nu D_\nu [c_\nu \hat{M}^1_\nu(k_1\hat{r}) + d_\nu \hat{N}^1_\nu(k_1\hat{r})] \tag{16d}$$

$$\hat{H}^2(\hat{r}) = -j(\epsilon_2/\mu_0)^{1/2} \sum_\nu D_\nu [\tau_\nu \hat{N}^1_\nu(k_2\hat{r}) + \delta_\nu \hat{M}^1_\nu(k_2\hat{r}) \alpha_\nu \hat{N}^3_\nu(k_2\hat{r}) + \beta_\nu \hat{M}^3_\nu(k_2\hat{r})] \tag{16e}$$

$$\vec{H}^1(\vec{r}) = -j(\epsilon_1/\mu_0)^{1/2} \sum_\nu D_\nu [c_\nu \vec{N}^1_\nu(k_1\vec{r}) + d_\nu \vec{M}^1_\nu(k_1\vec{r})] \quad (16f)$$

The following relations were used to determine Equations 16e and 16f from Equations 16c and 16d respectively (13:715):

$$\vec{H} = -\frac{j}{\omega\mu_0} \nabla \times \vec{E} \quad (17a)$$

$$\vec{M} = \frac{1}{k} \nabla \times \vec{N} \quad (17b)$$

$$\vec{N} = \frac{1}{k} \nabla \times \vec{M} \quad (17c)$$

Substituting Equations 16 into Equations 10 and 11 and truncating the summations over ν at some upper index N enables us to numerically solve for the scattered field expansion coefficients, f and g, in terms of incident field coefficients, a and b.

$$\begin{bmatrix} f \\ g \end{bmatrix} = -[T] \begin{bmatrix} a/4 \\ b/4 \end{bmatrix} \quad (18)$$

[T] is the 2N x 2N T-matrix containing the scatterer information. It is given by

$$[T] = \{[Q_2^{11}] - [Q_2^{13}][D][Q_1^{11}][Q_1^{31}]^{-1}[D]^{-1}\}$$

$$\cdot\{[Q_2^{31}] - [Q_2^{33}][D][Q_1^{11}][Q_1^{31}]^{-1}[D]^{-1}\}^{-1} \quad (19)$$

where the following notation has been used:

$$[Q_i^{pq}] = \begin{bmatrix} K_i^{pq} + (\epsilon_{r_i})^{1/2} J_i^{pq} & L_i^{pq} + (\epsilon_{r_i})^{1/2} I_i^{pq} \\ I_i^{pq} + (\epsilon_{r_i})^{1/2} L_i^{pq} & J_i^{pq} + (\epsilon_{r_i})^{1/2} K_i^{pq} \end{bmatrix} \tag{20a}$$

$$[I_i^{pq}]_{\mu\nu} = \frac{k_{i+1}^2}{\pi} \int_{S_i} \hat{n}_i \cdot \vec{M}_\mu^p(k_{i+1}\hat{r}) \times \vec{M}_\nu^q(k_i\hat{r}) ds \tag{20b}$$

$$[J_i^{pq}]_{\mu\nu} = \frac{k_{i+1}^2}{\pi} \int_{S_i} \hat{n}_i \cdot \vec{M}_\mu^p(k_{i+1}\hat{r}) \times \vec{N}_\nu^q(k_i\hat{r}) ds \tag{20c}$$

$$[K_i^{pq}]_{\mu\nu} = \frac{k_{i+1}^2}{\pi} \int_{S_i} \hat{n}_i \cdot \vec{N}_\mu^p(k_{i+1}\hat{r}) \times \vec{M}_\nu^q(k_i\hat{r}) ds \tag{20d}$$

$$[L_i^{pq}]_{\mu\nu} = \frac{k_{i+1}^2}{\pi} \int_{S_i} \hat{n}_i \cdot \vec{N}_\mu^p(k_{i+1}\hat{r}) \times \vec{N}_\nu^q(k_i\hat{r}) ds \tag{20e}$$

$$(\epsilon_{r_i})^{1/2} = (\epsilon_i)^{1/2} / (\epsilon_{i+1})^{1/2} \tag{20f}$$

Normalization constants are contained within the diagonal matrix [D].

Different scattering quantities can be calculated after determining scattered field coefficients f and g. The vector-far-field scattered field amplitude $\vec{F}$ can be found from the following relationship:

$$\vec{E}^s(k\hat{r}) = \vec{F}(\theta_s, \phi_s; \theta_i, \phi_i) \frac{\exp(jkr)}{r}; \text{ as } kr \to \infty \tag{21}$$

where (θ_s, ϕ_s) is the scattered field direction and (θ_i, ϕ_i)

is the incident field direction. Other calculable quantities include differential scattering cross section (DSCS), extinction cross section (σ_{ext}), scattering cross section (σ_{sc}) and absorption cross section (σ_{abs}). These quantities are obtainable from

$$DSCS = \left|\vec{F}(\theta_s,\phi_s;\theta_i,\phi_i)\right|^2 \tag{22a}$$

$$\sigma_{ext} = \frac{4\pi}{k}Im[\hat{e}_0\cdot\vec{F}(\theta_i,\phi_i;\theta_i,\phi_i)] \tag{22b}$$

$$\sigma_{sc} = \frac{16\pi}{k^2}\sum_{\nu} D_\nu[\left|f_\nu\right|^2 + \left|g_\nu\right|^2] \tag{22c}$$

$$\sigma_{abs} = \sigma_{ext} - \sigma_{sc} \tag{22d}$$

where $\hat{e}$ is the polarization vector of the incident field. Other quantities, such as radar cross section, can also be calculated from scattered field coefficients f and g.

Wang's Hailstone Model

The next chapter will discuss the scattering characteristics of Wang's three parameter hailstone representation. This section provides some physical insight for the model itself.

The following mathematical expression describes a curve that becomes the surface of Wang's hailstone model when rotated about the z-axis (16):

$$x = a[1-(z^2/c^2)]^{1/2}\cos^{-1}(z/\lambda c) \qquad (23)$$

where

x = horizontal coordinate

z = vertical coordinate

a = L/π (L is hailstone width along x-axis)

c = half the hailstone height

λ = dimensionless shape factor

Figure 5 illustrates the quantities defined above.

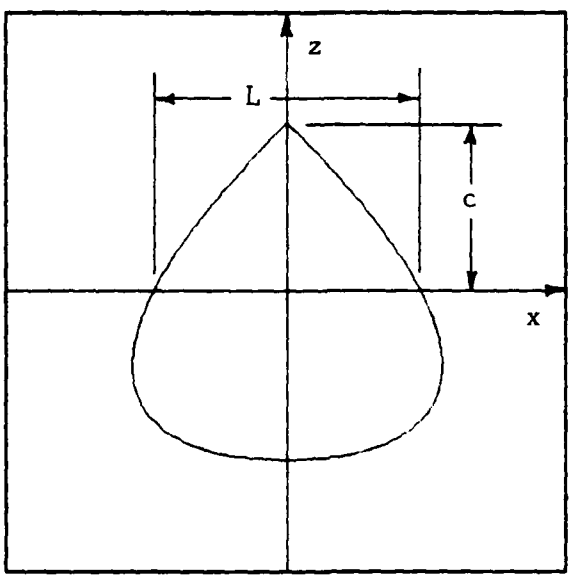

Figure 5. Wang's Hailstone Model

From Equation 23 and Figure 5 we can see how parameters a, c, and λ affect the shape of the hailstone. Increasing a while holding c and λ constant causes the hailstone to become broader along the x-axis. Increasing c causes elongation in the z direction. Parameter λ is more difficult to understand. Figure 5 was drawn with shape factor $\lambda = 1$. As λ increases, the hailstone rapidly becomes more spheroidal. Figures 6 and 7 show hailstones with $\lambda=2$ and $\lambda=10$ respectively. Parameters a and c are constant for Figures 5 through 7.

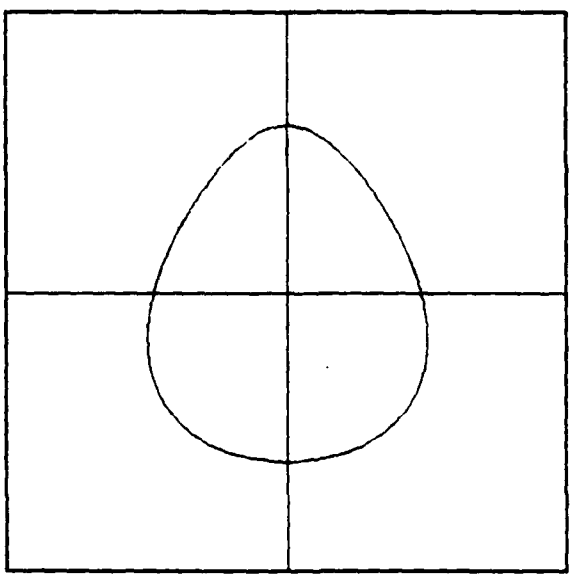

Figure 6. Hailstone Model $\lambda=2$

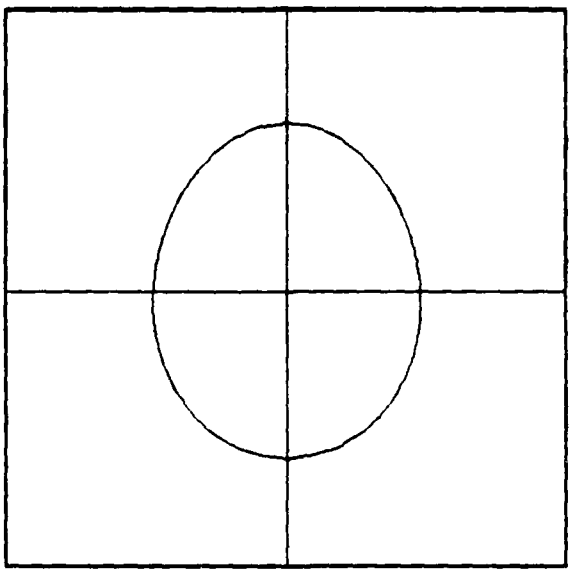

Figure 7. Hailstone Model λ=10

A sample consisting of 679 hailstones was collected and analyzed using Wang's hailstone representation (16). Figures 8, 9, and 10 show the distribution of parameters a, c and λ, respectively, for the sample. The (a) parameter varied in size from about 0.15 to 0.65 cm for the sample. Approximately one-third of the hailstones had an (a) parameter between 0.25 - 0.3 cm. Parameter (c) varied from 0.3 to 0.9 cm with the interval 0.5 to 0.6 cm containing greater than one-third of the sample. Shape parameter, (λ), varied from 1 to 10. Half the hailstone sample had a shape parameter (λ) between 1 and 2 (16).

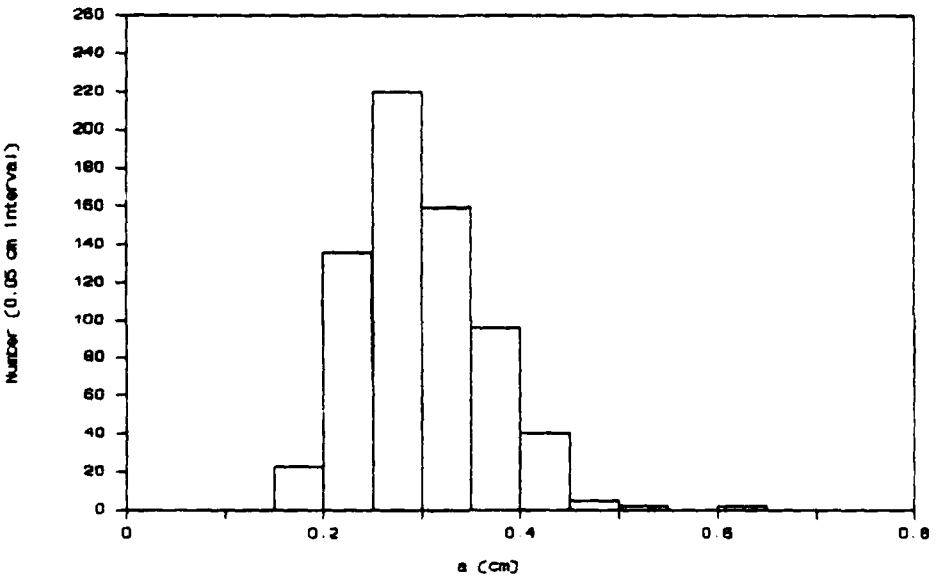

Figure 8. The a-distribution (16:1064)

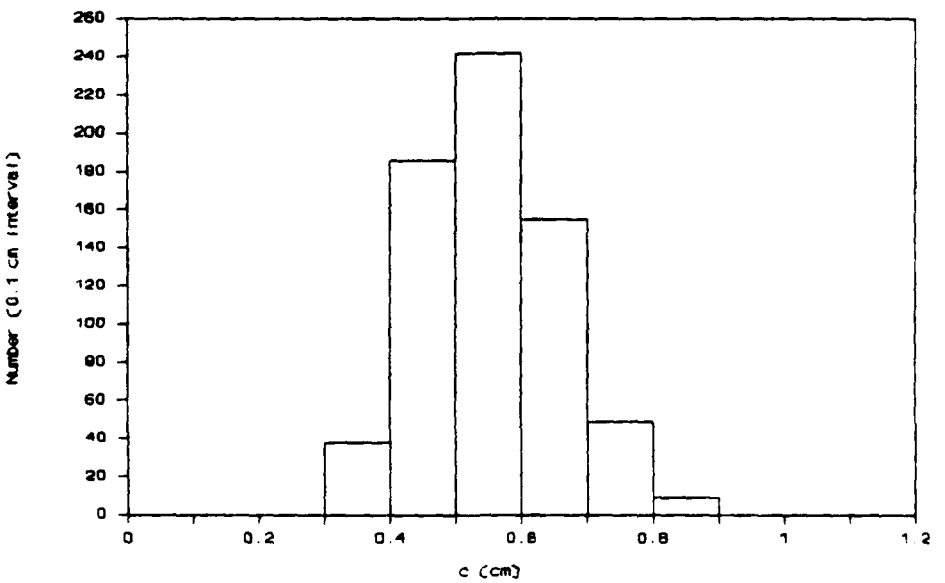

Figure 9. The c-distribution (16:1064)

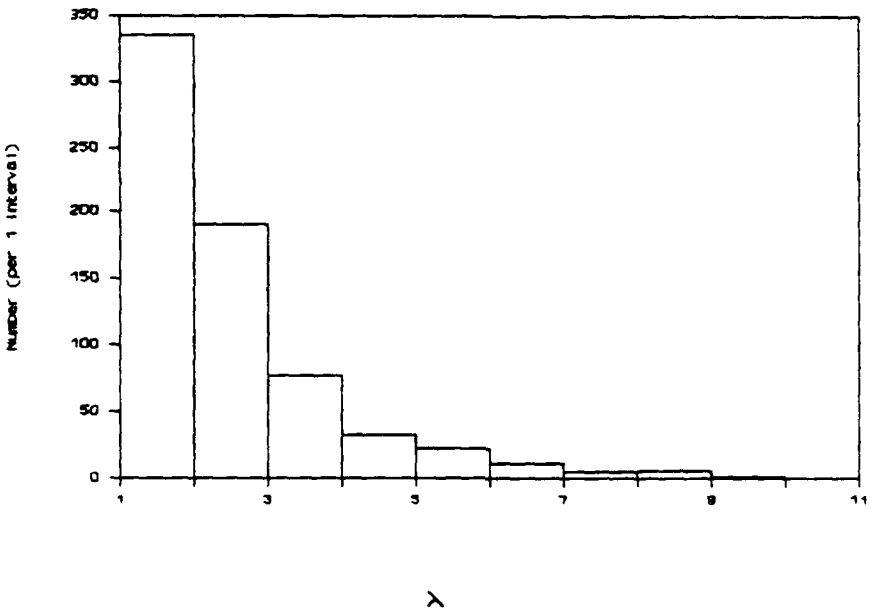

Figure 10. The λ-distribution (16:1066)

The melting hailstones are modeled as ice layered with varying thicknesses of water. The outer dimensions of the layered models are held constant as thickness (t) is varied. Water layer thickness (t) is shown in Figure 11. No experimental data are available for parameter (t). Scattering by melting hailstones will be considered in the next chapter.

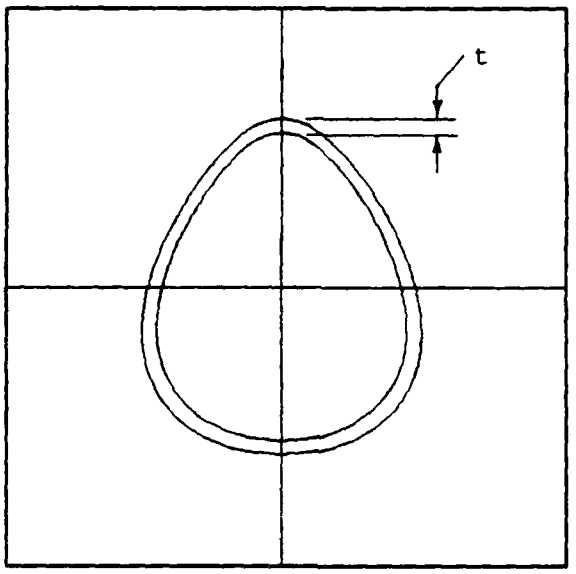

Figure 11. Layered Hailstone Model

This chapter summarized the EBCM theory for a layered scatterer. The T-matrix for determining scattered field coefficients from incident field coefficients was presented and calculable scattering quantities were discussed. Size and shape characteristics of Wang's hailstone model were also presented. The next chapter examines how scattering characteristics of the hailstone models change as the model parameters are varied.

IV. Results

Overview

This chapter presents and discusses scattering characteristics of Wang's hailstone model. An existing EBCM computer program for determining scattering by spheroids was modified to obtain the scattering plots for Wang's model. Scattering information is presented for a sample of hailstone models at 3 and 30 GHz.

Program Modification

Dr. Peter Barber from the Department of Electrical and Computer Engineering at the Clarkson College of Technology provided computer code for calculating scattering by layered and nonlayered dielectric spheroids using the EBCM. Documentation and sample computer runs were provided with the FORTRAN code. The sample computer runs included input and output for a nonlayered prolate spheroid.

The program was compiled on the AFIT Hercules computer system. The Hercules is a Digital Equipment Corporation VAX-11/785 supercomputer running the VMS operating system. The prolate spheroid test cases were run and verified.

The code provided by Dr. Barber determines scattering by spheroidal dielectric objects. Spheroids are axisymmetric as well as mirror symmetric. Top and bottom halves of mirror symmetric objects have the same physical

dimensions. Figure 12 illustrates mirror and nonmirror symmetry. The Wang hailstone model is axisymmetric but generally not mirror symmetric. Dr. Barber's programs were modified for nonmirror symmetric objects to determine the scattering characteristics of the Wang model.

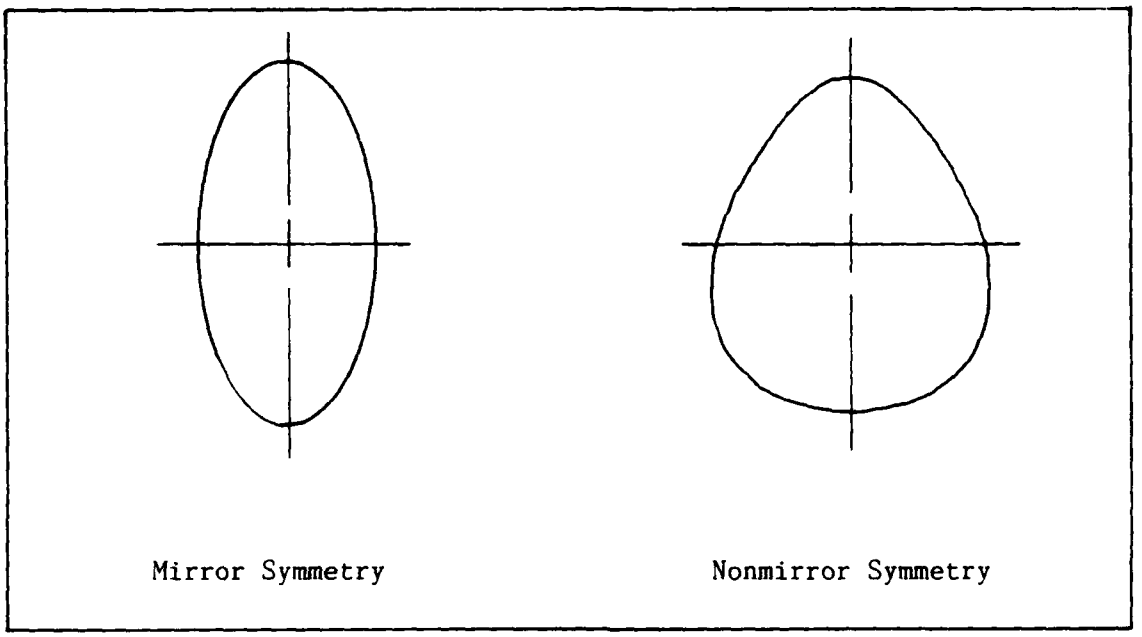

Figure 12. Mirror and Nonmirror Symmetry

Several test cases were run to verify the nonmirror symmetric code. The original prolate spheroid test case produced the same result and Aydin and Seliga's results were duplicated. Aydin and Seliga examined differential radar scattering properties of several hailstone models (1:58-66). The hailstone models examined include layered and nonlayered oblate spheroids, nonlayered sphere-cone-spheres, and nonlayered sphere-cone-oblate spheroids. The sphere-cone-

sphere and sphere-cone-oblate spheroidal hailstone models are nonmirror symmetric. A sample of Aydin and Seliga's work was duplicated and is presented in Appendix A.

The programs provided by Dr. Barber were capable of computing up to 20-by-20 T-matrices. This corresponds to truncating the field expansions at a maximum N value of 10. Larger N values were needed to compute the T-matrices for the Wang hailstone models. In general, as scatterer size, asymmetry and dielectric constant increase the required N and resulting T-matrix size increase. The programs were modified to compute T-matrices for a maximum N value of 40. Complex double precision was also necessary to compute the spherical Bessel functions. Computing time increases significantly with increasing N. The AFIT ELXSI 6400 was used for N values greater than 20 due to its faster and more precise fortran code execution. A brief description of the final code used in this thesis is included in Appendix B.

Coordinate System

Figure 13 shows the coordinate system used in this analysis. The incident wave is linearly polarized and propagates in the +z-direction. In general, the polarization vector of the incident wave lies in the xy-plane and is specified by magnitude, A, and angle, ψ, from the x-axis. For this analysis, the polarization vector of the incident wave is fixed with A = 1 and ψ = 0 degrees.

The orientation of the scatterer is specified by angles

Θ and ϕ where S is the axis of symmetry of the scatterer. The top of the scatterer is in the +S-direction. The center of the scatterer is located at the origin of the coordinate system. The scatterer is fixed at $\Theta = \phi = 90$ degrees for horizontal polarization calculations and $\Theta = 90$ degrees, $\phi = 0$ degrees for vertical polarization calculations.

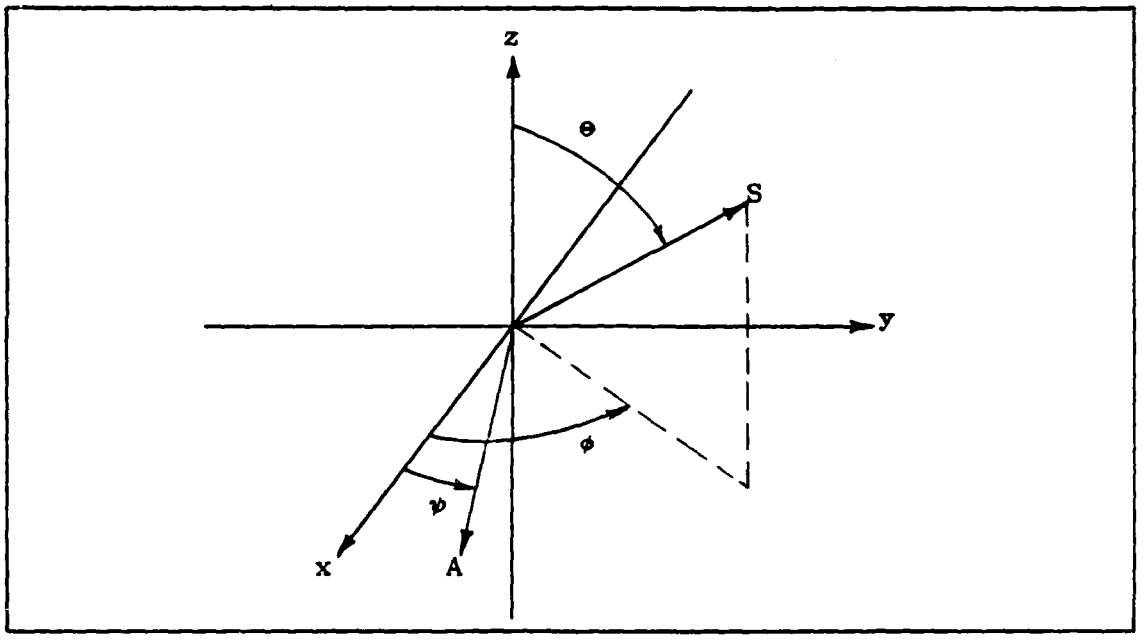

Figure 13. Coordinate System

The scattered field is evaluated in xz-plane with 0 degrees in the forward or +z-direction and 180 degrees in the backscattered or -z-direction. The scattering angle is equal to 90 degrees at the +x-axis.

Graphical Results

Scattering characteristics of various hailstone models were calculated at two frequencies: 3 GHz and 30 GHz. The

results are presented in graphical form in this section. The hailstone models are denoted by W(a,c,λ,t) where a, c, λ, and t are the Wang hailstone parameters defined in the previous chapter. Parameters a, c, and t are given in cm and λ is dimensionless.

Scattering at 3 GHz. At 3 GHz, the wavelength of the incident wave is 10 cm. The relative dielectric constants used for ice and water at 3 GHz are 3.1698 + j0.003788 and 79.6918 + j25.1975 respectively (12:1837-1840). In this section, scattering characteristics of the nonmirror symmetric nonlayered and layered Wang hailstone models are compared to the scattering characteristics of corresponding equivolume spheres. Effects of different layer thicknesses and scatterer sizes are also presented.

Figure 14 shows Wang model W(0.3,0.6,2,0) and an equivolume sphere. Figure 15 shows normalized DSCS vs. scattering angle for the two hailstone models at horizontal polarization. Normalization is with respect to πc^2. The largest scattering differences occur in the forward and backscattered directions where the DSCS of the Wang model is about 1.5 dB below that of the sphere.

Figure 16 shows Wang model W(0.3,0.6,2,0.05). Figure 17 shows normalized DSCS vs. scattering angle for W(0.3,0.6,2,0.05) and an equivolume layered sphere at horizontal polarization. Uniform water layer thickness for the equivolume sphere is approximately 0.05 cm. The DSCS is greater for the layered models than for the homogeneous

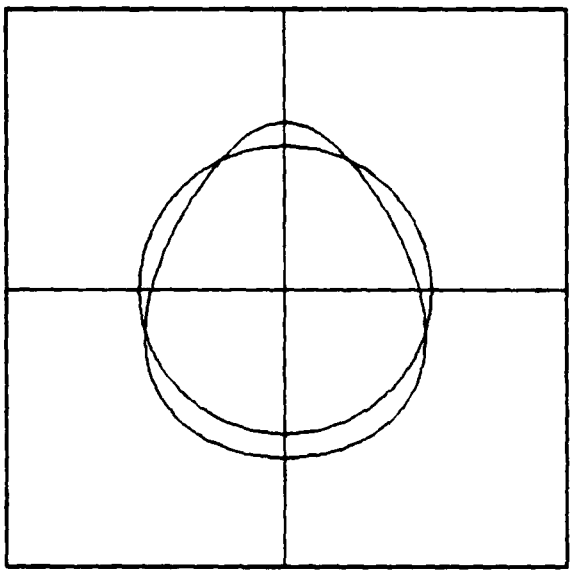

Figure 14. Wang Model W(0.3,0.6,2,0) and Equivolume Sphere

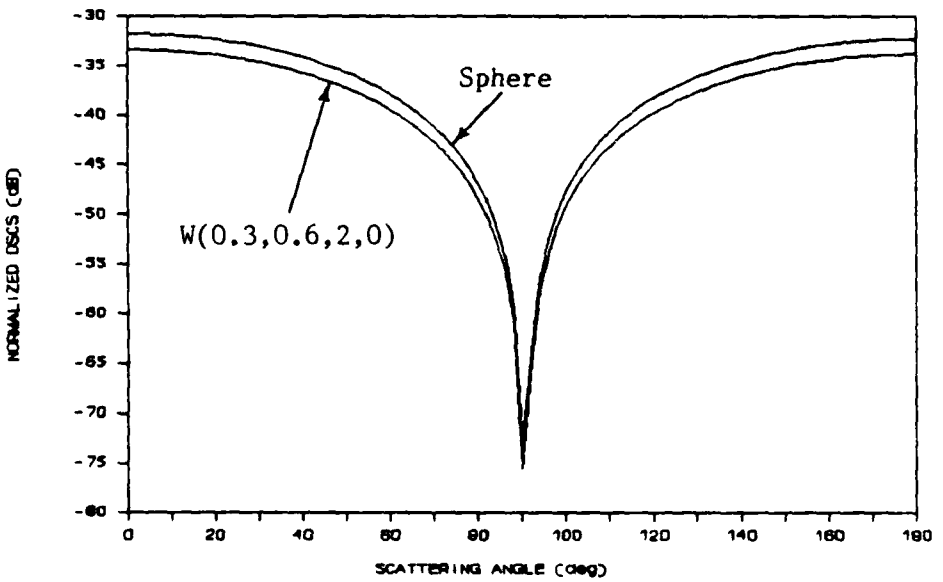

Figure 15. Normalized DSCS vs. Scattering Angle for W(0.3,0.6,2,0) and Equivolume Sphere

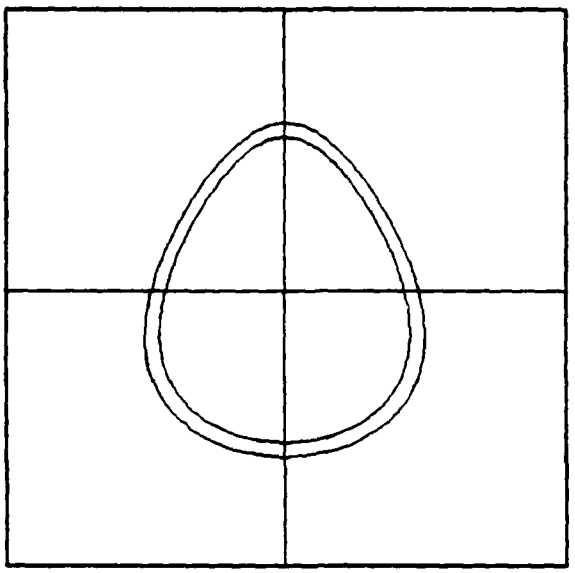

Figure 16. Wang Model W(0.3,0.6,2,0.05)

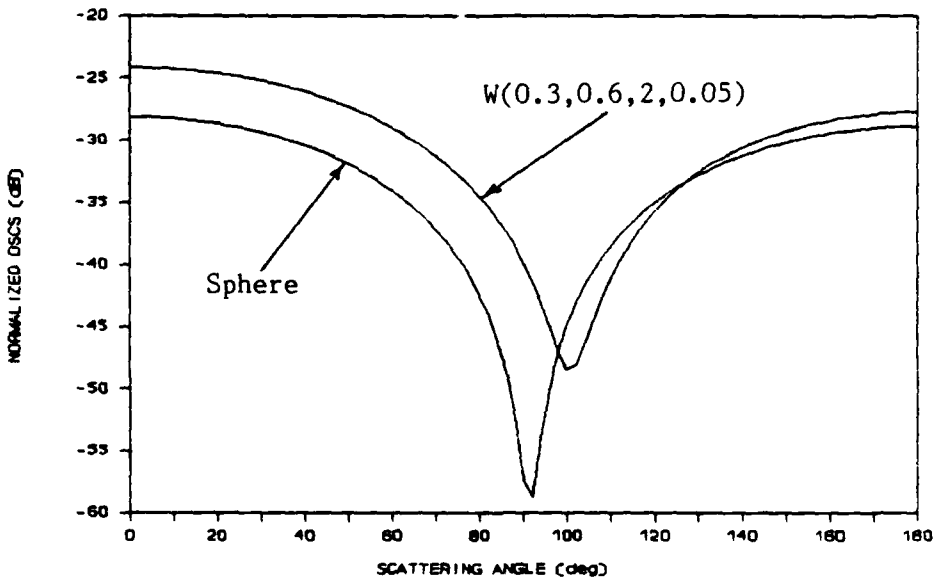

Figure 17. Normalized DSCS vs. Scattering Angle for W(0.3,0.6,2,0.05) and Equivolume Sphere

models in Figure 15. Forward scattering differences are more significant than in the backscattered direction. The minimum return from the Wang model is about 10 dB greater and 10 degrees to the right of the equivolume sphere's minimum return.

Figure 18 shows DSCS vs. scattering angle at horizontal polarization for three different hailstone models. The external dimensions of the models are the same while water layer thickness varies from 0 to 0.02 to 0.05 cm. As water thickness increases, DSCS increases and the minimum DSCS moves in the backscattered direction. The forward scattering characteristics are more affected by the layer thickness than are the backscattered characteristics.

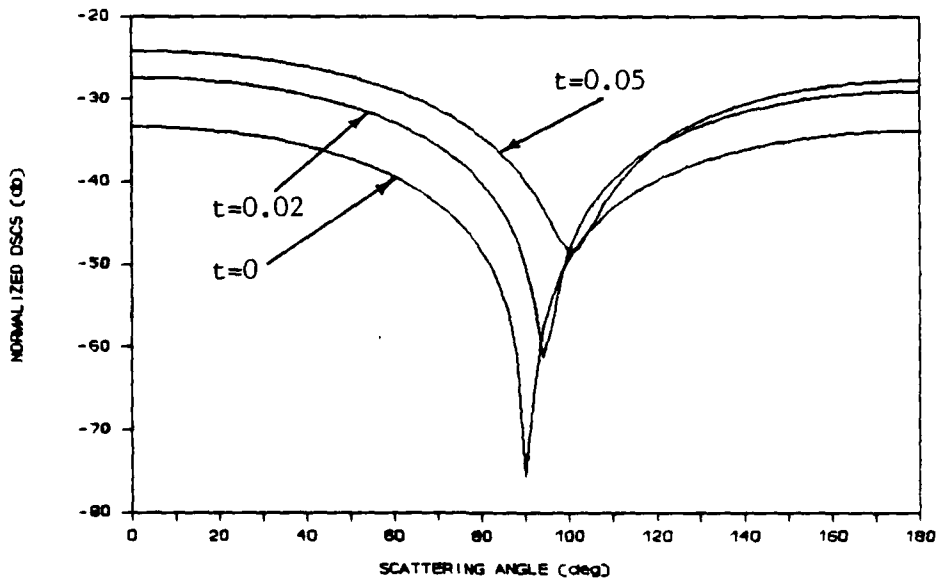

Figure 18. Normalized DSCS vs. Scattering Angle for W(0.3,0.6,2,t)

Figure 19 shows Wang models W(0.15,0.3,2,0), W(0.3,0.6,2,0), and W(0.45,0.9,2,0). The general shape of the three nonlayered models remains constant as their physical dimensions increase. Figure 20 shows DSCS vs. scattering angle at horizontal polarization as scatterer size varies. DSCS increases with increased scatterer size.

All plots in the above section were for a horizontally polarized incident wave. Although not shown, the vertically polarized scattering characteristics were essentially the same as the horizontally polarized scattering characteristics.

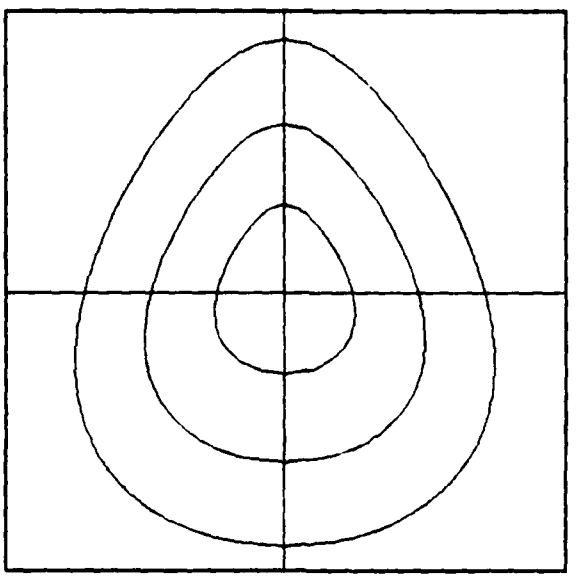

Figure 19. Wang Models W(0.15,0.3,2,0), W(0.3,0.6,2,0) and W(0.45,0.9,2,0)

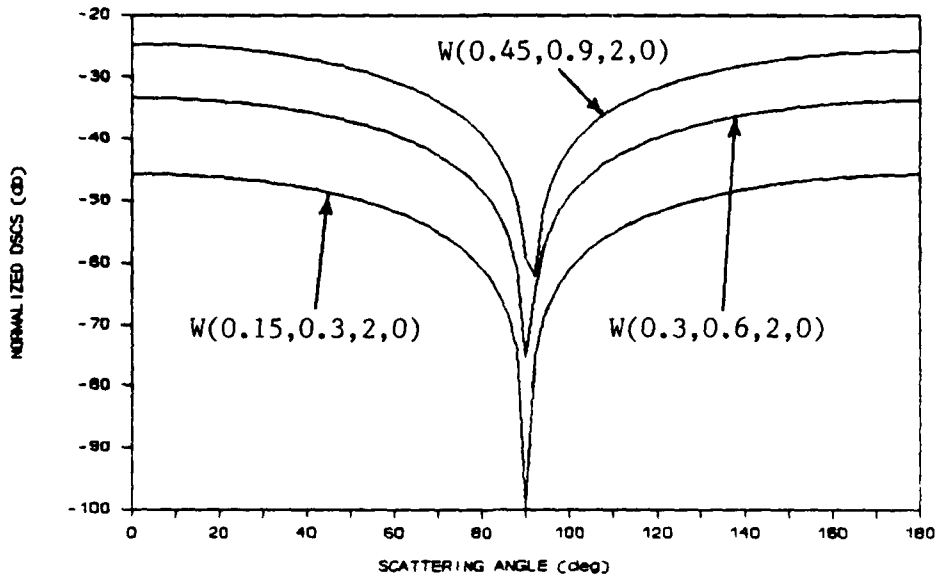

Figure 20. Normalized DSCS vs. Scattering Angle for W(0.15,0.3,2,0), W(0.3,0.6,2,0) and W(0.45,0.9,2,0)

Scattering at 30 GHz. At 30 GHz, the wavelength of the incident wave is 1 cm. The relative dielectric constants used for ice and water at 30 GHz are 3.1684 + j0.0007352 and 11.9194 + j22.5613 respectively (12:1837-1840). In this section, scattering characteristics of the nonmirror symmetric nonlayered and layered Wang hailstone models are compared to the scattering characteristics of corresponding equivolume spheres. Effects of different layer thicknesses and scatterer sizes are also presented. Forward and backward scattering quantities are plotted with respect to angle of incidence. Normalization of all scattering

quantities are with respect to πc^2.

Figure 21 shows Wang model W(0.45,0.9,4,0) and an equivolume sphere. Figure 22 plots normalized DSCS vs. scattering angle for W(0.45,0.9,4,0) and an equivolume ice sphere at horizontal polarization. Water layer thickness for the equivolume sphere is approximately 0.05 cm. DSCS varies greatly over the range of scattering angles. Backscattered DSCS is affected more by the scatterer shape than the forward DSCS.

Figure 23 shows Wang model W(0.45,0.9,4,0.05). Figure 24 shows normalized DSCS vs. scattering angle for W(0.45,0.9,4,0.05) and an equivolume sphere at horizontal polarization. The DSCS is very different for all scattering angles. Backscattered DSCS differs by 18 dB and forward DSCS differs by 8 dB.

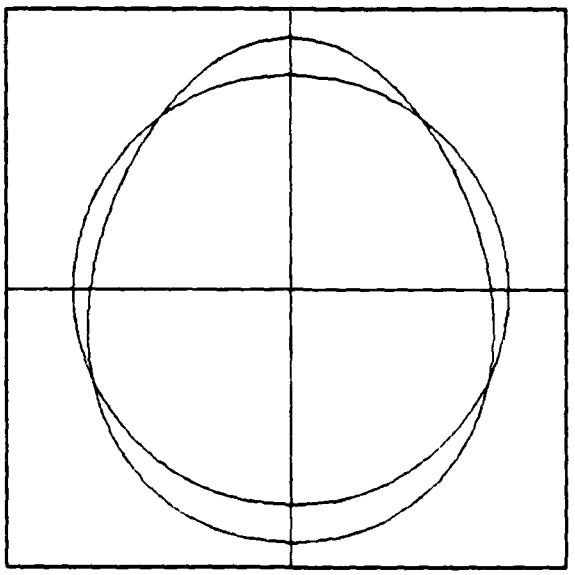

Figure 21. Wang Model W(0.45,0.9,4,0) and Equivolume Sphere

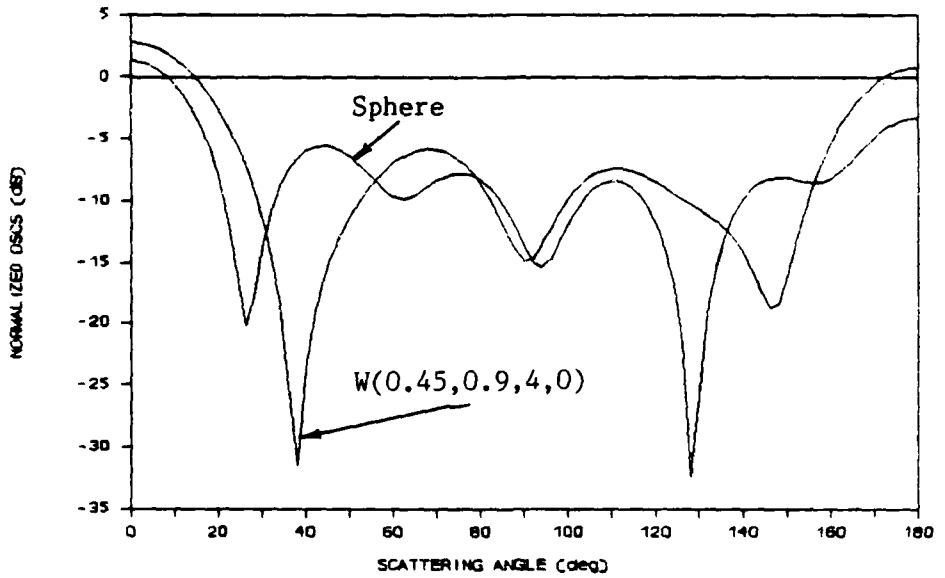

Figure 22. Normalized DSCS vs. Scattering Angle for W(0.45,0.9,4,0) and Equivolume Sphere

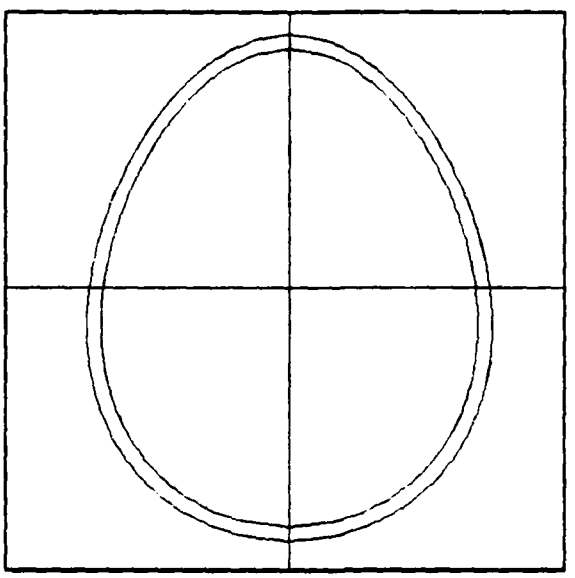

Figure 23. Wang Model W(0.45,0.9,4,0.05)

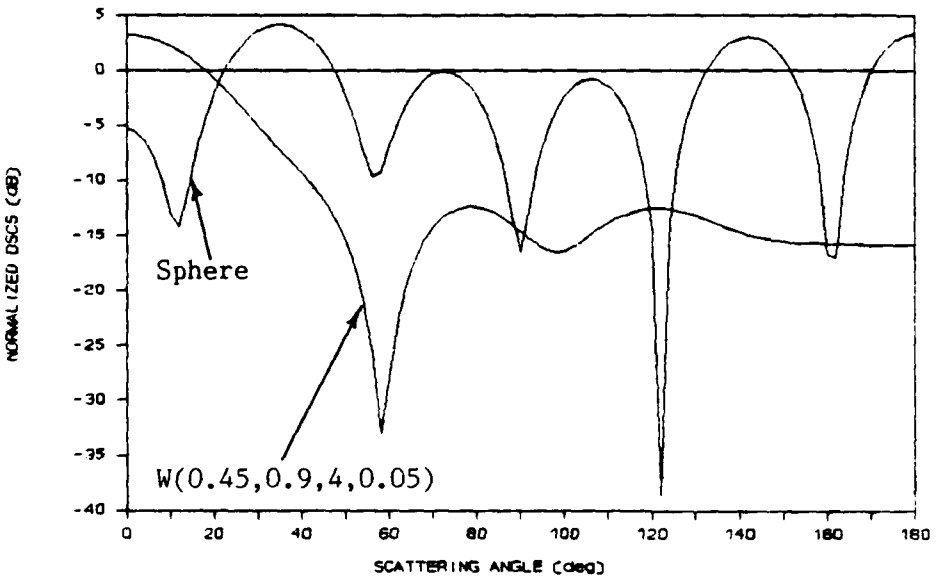

Figure 24. Normalized DSCS vs. Scattering Angle for W(0.45,0.9,4,0.05) and Equivolume Sphere

Figure 25 shows Wang model W(0.45,0.9,2,0.02). Figures 26 and 27 show normalized DSCS vs. scattering angle for W(0.45,0.9,2,t) for t = 0, 0.02, and 0.05 at horizontal and vertical polarizations respectively. The forward DSCS does not vary significantly as water thickness changes. Backward DSCS varies greatly with layer thickness. Forward scattering is similar for horizontal and vertical polarizations. Except for the forward direction, horizontal and vertical polarizations bear little resemblance.

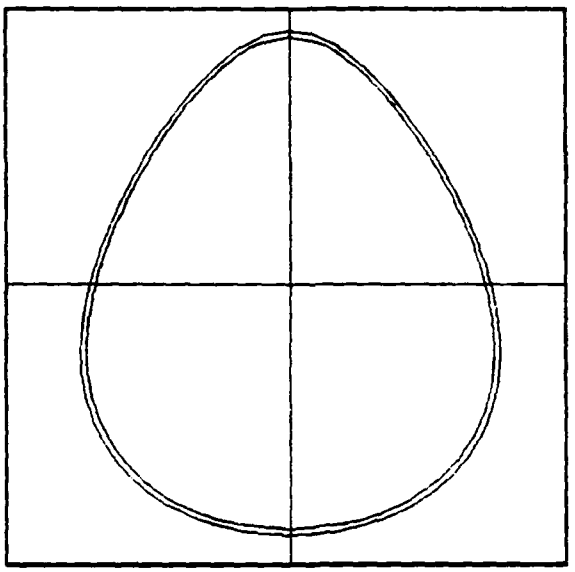

Figure 25. Wang Model W(0.45,0.9,2,0.02)

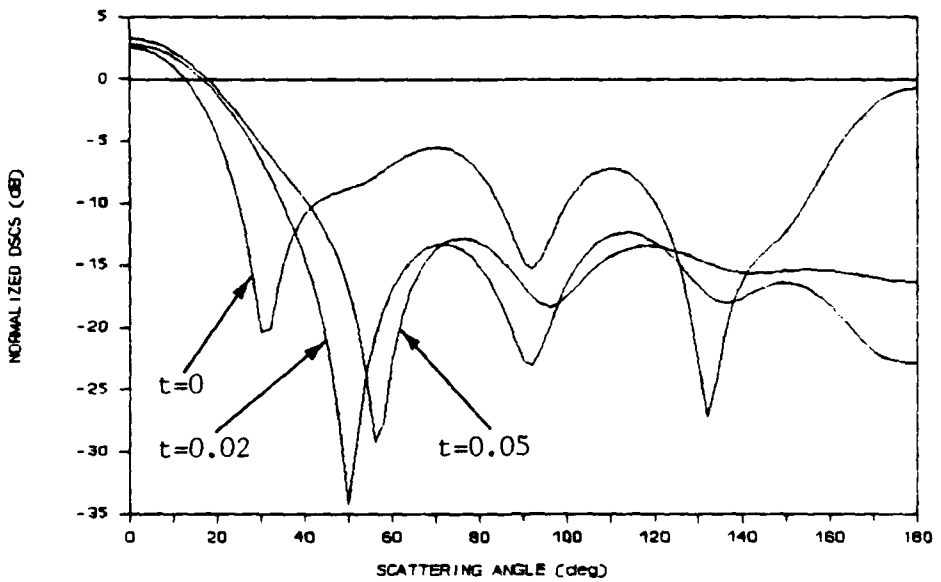

Figure 26. Normalized DSCS vs. Scattering Angle for W(0.45,0.9,2,t) Horizontal Polarization

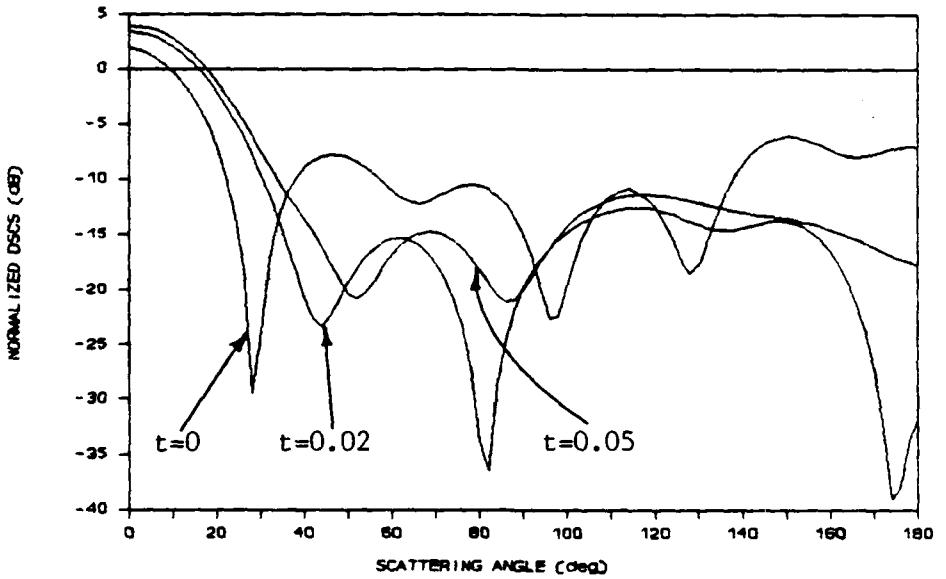

Figure 27. Normalized DSCS vs. Scattering Angle for W(0.45,0.9,2,t) Vertical Polarization

Figures 28 and 29 show normalized DSCS vs. angle of incidence for W(0.45,0.9,2,t) in the backward and forward directions respectively. The incident wave impinges on the top of the hailstone for an angle of incidence equal to 0 degrees. At 90 degrees, the incident wave approaches the hailstone's broadside. The incident wave impinges on the bottom of the hailstone model at 180 degrees. Backscattered DSCS is varies as much as 28 dB depending on the angle of incidence and layer thickness, t. Forward DSCS is much less sensitive and varies only about 2.5 dB.

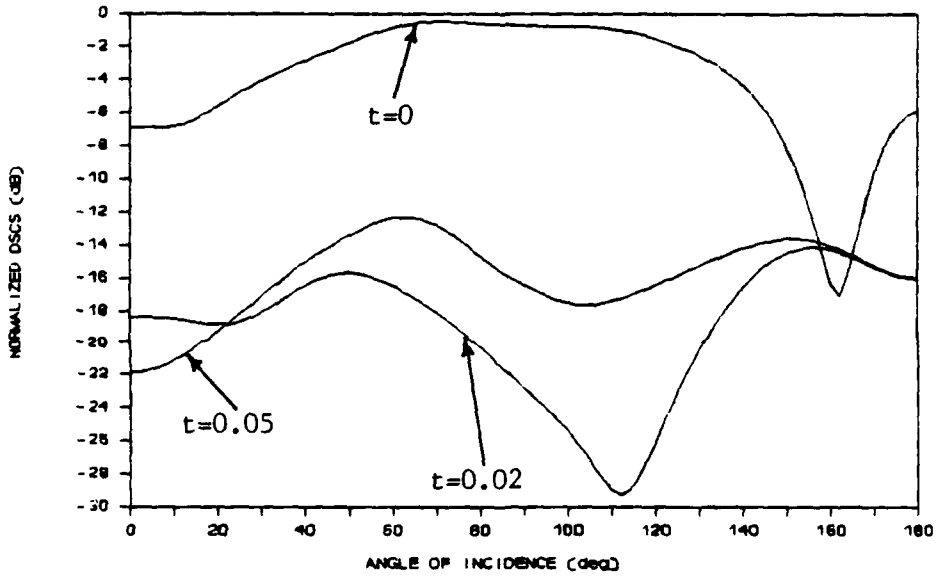

Figure 28. Backward Normalized DSCS vs. Angle of Incidence for W(0.45,0.9,2,t) Horizontal Polarization

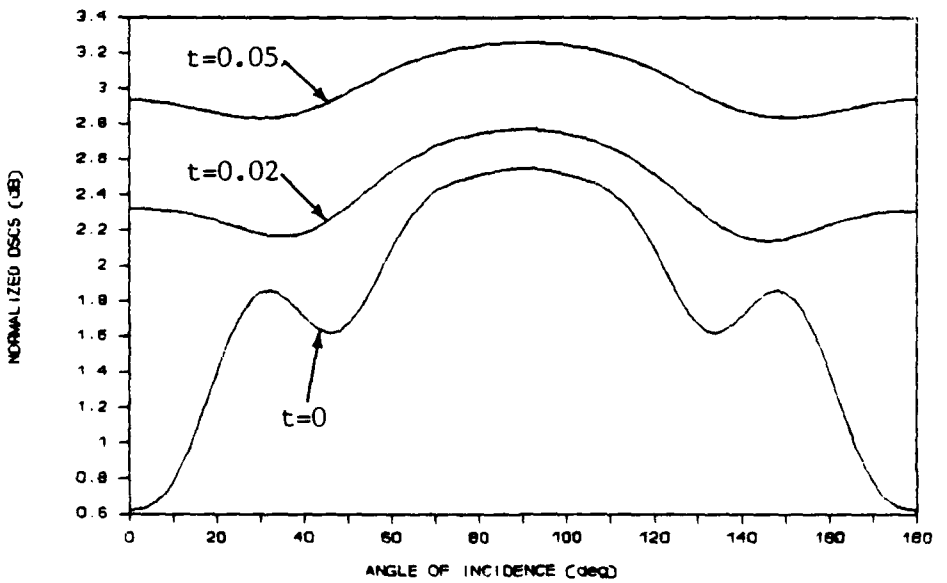

Figure 29. Forward Normalized DSCS vs. Angle of Incidence for W(0.45,0.9,2,t) Horizontal Polarization

The scattering characteristics in the next five graphs are presented as functions of scatterer size. Hailstone parameter c increases from 0.3 to 0.9 cm; parameter a simultaneously increases from 0.15 to 0.45 cm. The general shape of the hailstone models do not change as size increases.

Figures 30 and 31 show how forward and backward DSCS changes with increasing scatterer size. The forward DSCS of the nonlayered hailstone model is 2-3 dB greater than the layered model over most of the size range. Backward scatter increases with increased scatterer size for the nonlayered hailstone model. The layered model's backward DSCS exhibits a lobed behavior with increased scatterer size.

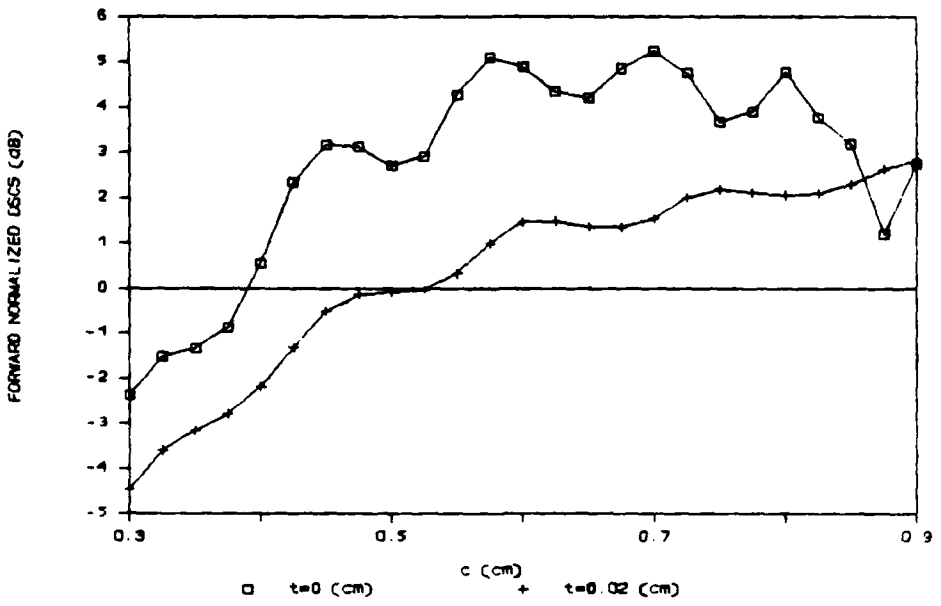

Figure 30. Forward Normalized DSCS vs. Scatterer Size for W(c/2,c,4,t) Horizontal Polarization

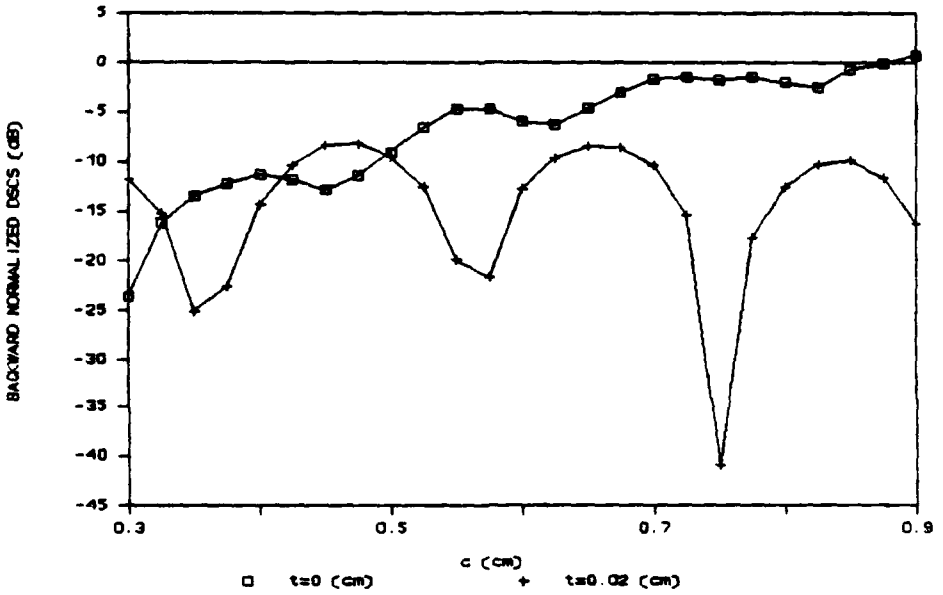

Figure 31. Backward Normalized DSCS vs. Scatterer Size for W(c/2,c,4,t) Horizontal Polarization

Figures 32, 33 and 34 show scattering, absorption, and extinction cross sections, respectively, vs. scatterer size for horizontal polarization. Extinction and scattering cross sections for the layered model are generally less than for the nonlayered hailstone model. Absorption cross section is greater for the layered (ice and water)model than for the ice only nonlayered model. Absorption is greater for the layered model due to the large imaginary part of water's relative dielectric constant.

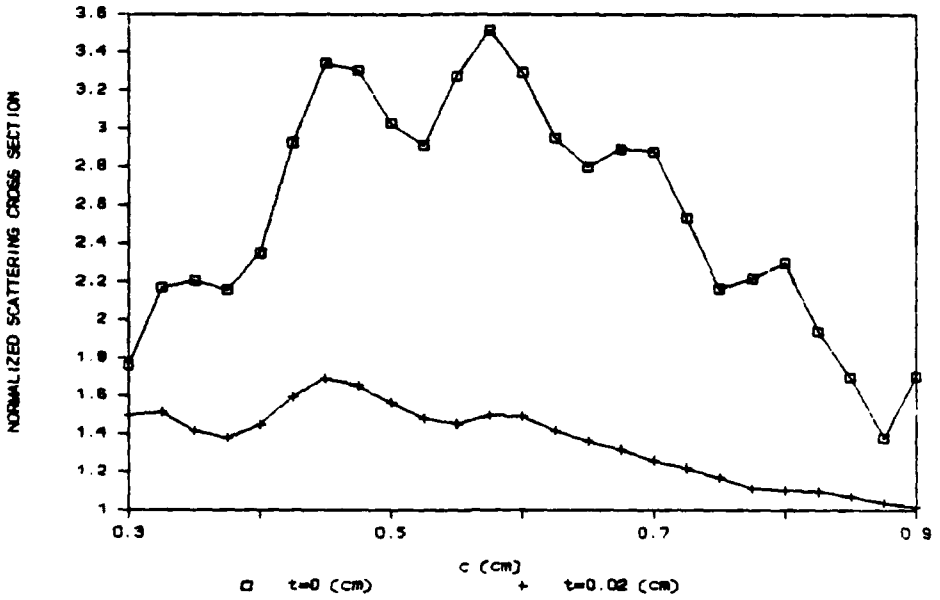

Figure 32. Normalized Scattering Cross Section vs. Scatterer Size for W(c/2,c,4,t) Horizontal Polarization

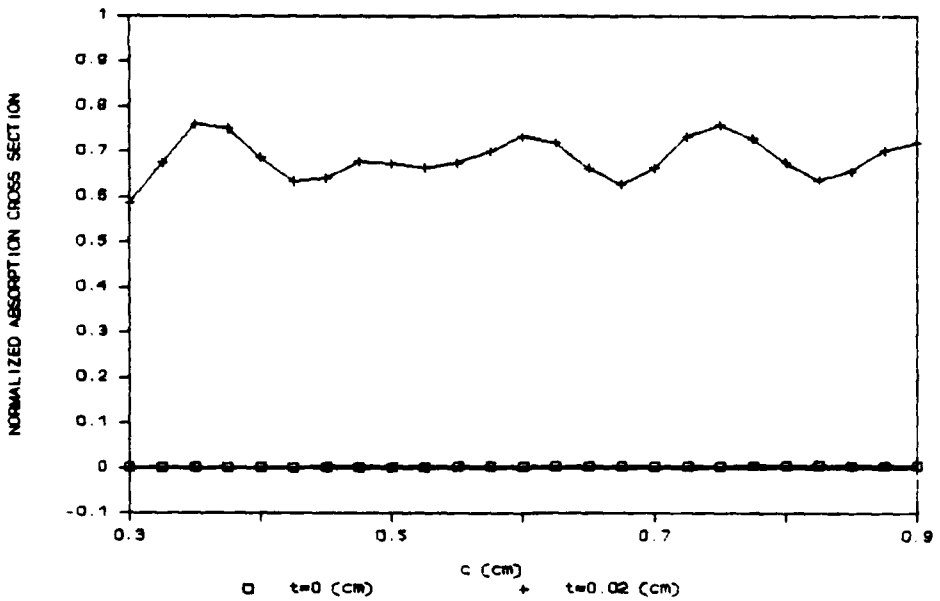

Figure 33. Normalized Absorption Cross Section vs. Scatterer Size for W(c/2,c,4,t) Horizontal Polarization

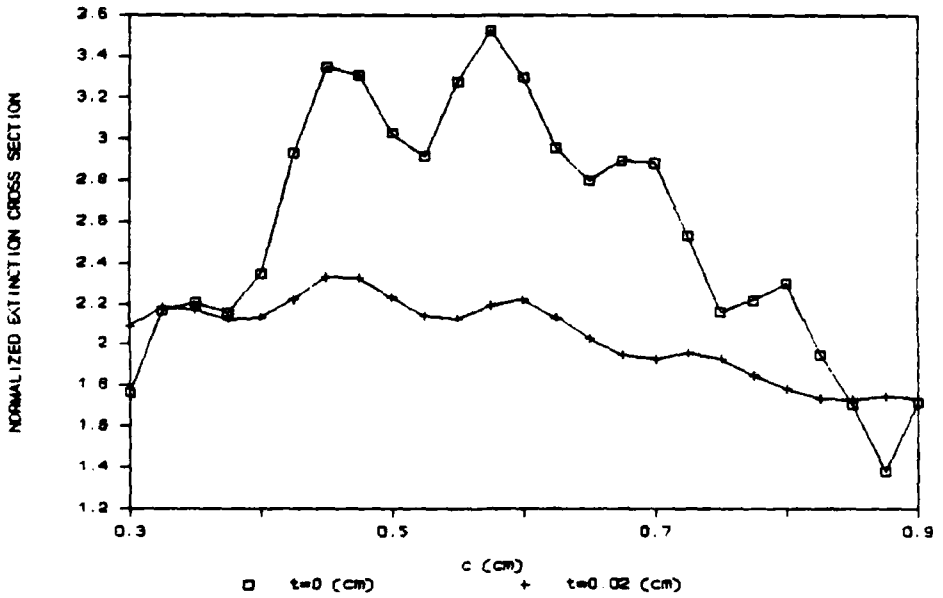

Figure 34. Normalized Extinction Cross Section vs. Scatterer Size for W(c/2,c,4,t) Horizontal Polarization

This chapter presented a sample of the scattering characteristics that can be calculated using the modified EBCM computer program. Scattering characteristics vary with incident wave frequency; hailstone model size, shape, and structure; observation angle; and angle of incidence of the illuminating wave. The scattering results are summarized and recommendations for future work are presented in the final chapter.

V. Conclusions and Recommendations

Introduction

This chapter summarizes the results of the preceding analysis and presents recommendations for future work in this area.

Conclusions

The EBCM was found to be well suited in determining the scattering characteristics of the Wang hailstone models considered. Conclusions are presented for each of the two incident wave frequencies examined.

Scattering at 3 GHz. Rayleigh scattering occurs at 3 GHz where wavelength is much larger than the hailstone models analyzed. The wavelength is 10 cm and the hailstone models varied in size from 0.6 to 1.8 cm in length along the axis of symmetry. Little phase variation of the incident wave occurs over the hailstone body. Hailstone shape was not a significant scattering parameter. Horizontal and vertical polarizations produced very similar results for the hailstone models examined at 3 GHz.

Different water layer thicknesses of the hailstone models produced significant forward and backward scattering characteristics. At 3 GHz the real part of dielectric constant of water, 79.6918, is much greater than that for ice, 3.1698. Thus, the impedance mismatch at the hailstone surface is much greater for the layered models than for the

ice only models. Forward and backward scattering is greater for the layered models than for the ice only models and increases with increased water thickness. Scattering at other scattering angles was also significantly affected by the water layer and thickness. The bistatic scattering minimum which occurred at 90 degrees for the nonlayered hailstone models moved in the backscattered direction as a water layer was introduced. The minimum moved further in the backscattered direction as water thickness is increased.

The shape of the nonlayered hailstone models did not affect scattering properties significantly. The Wang model and the equivolume ice sphere produced similar scattered fields. Hailstone shape was more important for the layered models. Scattering by the layered Wang model was significantly different than the scattering by the layered equivolume sphere. Scattering differences were most pronounced in the forward scattering direction.

Increasing nonlayered scatterer size produced larger scattered fields for all scattering angles.

Scattering at 30 GHz. Resonant scattering occurred at 30 GHz where wavelength and scatterer size were comparable. The phase of the incident radiation changes significantly over the hailstone length. The phase variations cause complex interactions between the different parts of the hailstones all of which must be considered in determining the scattered fields. Scattering characteristics are very

dependent on hailstone shape, size and structure. The resonant affects were evident is the scattering calculations for the different hailstone models. Scattering characteristics at 30 GHz were very dependant on incident wave polarization.

Scatterer shape was more important at 30 GHz than at 3 GHz. A nonlayered, nonmirror symmetric Wang model scattered the incident wave much differently than a corresponding equivolume nonlayered sphere. Differences were even more pronounced for the layered Wang model as compared to a equivolume layered sphere.

Scattering characteristics of Wang models changed significantly as a water layer was introduced and as water thickness was changed. Forward scattering was greater for the layered models than for the nonlayered models and generally increased with increased water thickness. As with scattering at 3 GHz, the bistatic scattering minimums moved in the backscattered direction as water layer thickness increased. Backward scattering changed significantly as the angle of incidence of the illuminating wave changed from the top to the bottom of the hailstone models. Forward scattering changed only slightly with angle of incidence. Again water thickness also affected scattering as angle of incidence varied.

The nonlayered Wang models generally scattered more of the incident energy than the layered models as scatterer

size increased. The layered models absorbed more energy than the nonlayered models due to the water layer's larger complex dielectric constant.

Hailstone model size, shape and structure greatly affect scattering characteristics at 30 GHz. Angle of incidence is also important particularly in backscattered directions.

Recommendations

Further research is necessary to determine the actual size, shape and composition of hailstones. The hailstone models examined in this thesis were constructed from data from one hailstorm in Colorado. A larger sample size may produce a more accurate hailstone model. Also, the distribution of water on the surface of the hailstones needs to be examined. The water thickness, if present, needs to be accurately modeled to obtain valid scattering calculations.

The distribution of hailstones along a propagating signal's path needs to be modeled. This thesis determined scattering characteristics by individual hailstones. This knowledge along with a hailstone distribution model would enable calculation of total scattering effects of hailstorms on propagating signals.

Research should be conducted to determine the usefulness of the EBCM for predicting the radar cross section of targets of interest to the Air Force. The EBCM

can be used to determine the radar cross section of resonant sized, dielectric coated, axisymmetric objects.

Appendix A: Differential Reflectivity of Hailstones Modeled as Oblate Spheroids and Sphere-Cone-Spheroids

This appendix contains differential reflectivity calculations for a sample of hailstone models used by Aydin and Seliga. Aydin and Seliga used the EBCM to determine the differential reflectivity of hailstones modeled as oblate spheroids and sphere-cone-spheroids at 10 cm wavelengths (1:58-66). A portion of Aydin and Seliga's work was duplicated to test the program used in this thesis.

Oblate Spheroid.

The differential reflectivity (Z_{DR}) radar parameter is given by $Z_{DR} = \sigma_H/\sigma_V$ where $\sigma_{H,V}$ are the backscatter cross sections at horizontal and vertical polarizations, respectively. Z_{DR} was calculated for various sizes of layered and nonlayered oblate spheroids. The oblate spheroidal hailstone model is shown in Figure 35.

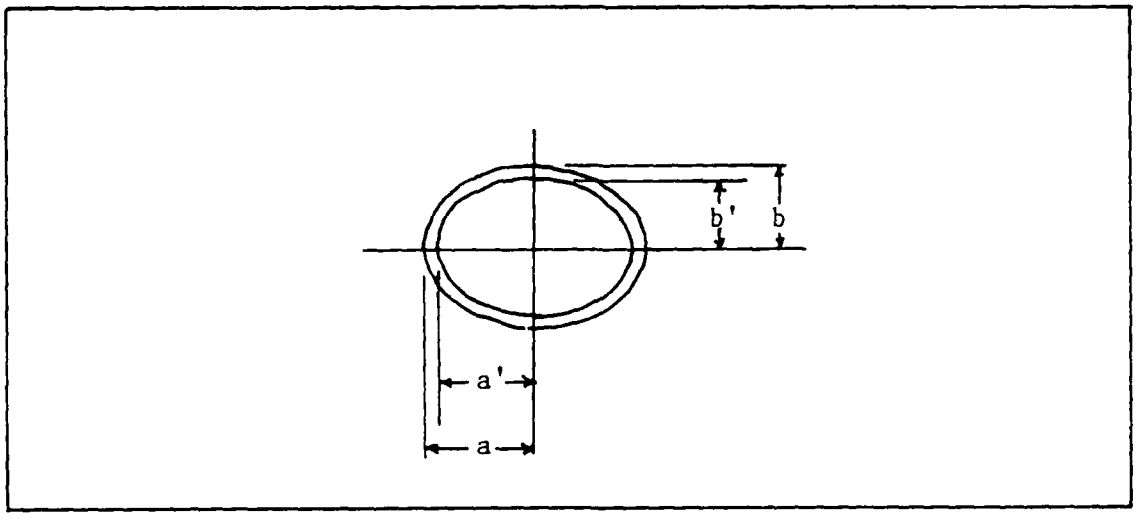

Figure 35. Oblate Spheroidal Hailstone Model

Figure 36 shows Z_{DR} vs. Equivolume Diameter (D) for layered and nonlayered oblate spheroidal hailstone models. D is the diameter of an equivolume sphere and is given by $D = 2a(b/a)^{1/3}$ where a and b are semiaxes of the spheroid. Water thickness (t) is 0 mm for the nonlayered model and 0.5 mm for the layered model. The axial ratios of the oblate spheroids are $b/a = b'/a' = 0.9$. The relative dielectric constants used for ice and water are $\epsilon_r = 3.1698 + j0.003788$ and $79.6918 + j25.1975$, respectively.

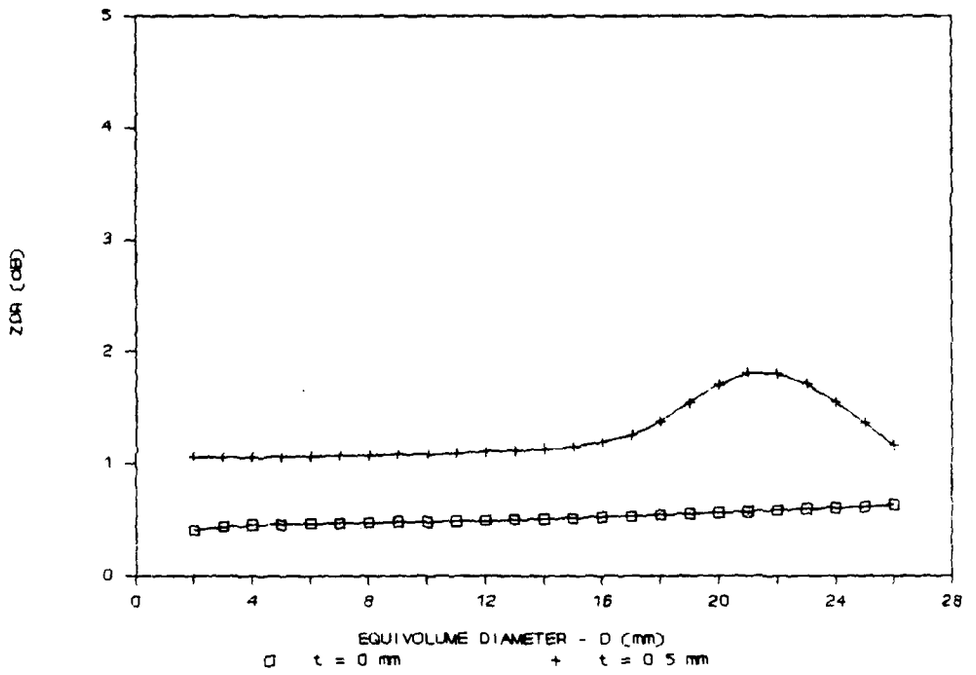

Figure 36. Z_{DR} vs. Equivolume Diameter for Oblate Spheroid

Sphere-Cone-Sphere.

Figure 37 shows the sphere-cone-sphere hailstone model. Parameter a is the radius of the base sphere. Parameter b is the radius of the apex sphere. Cone angle is given by α.

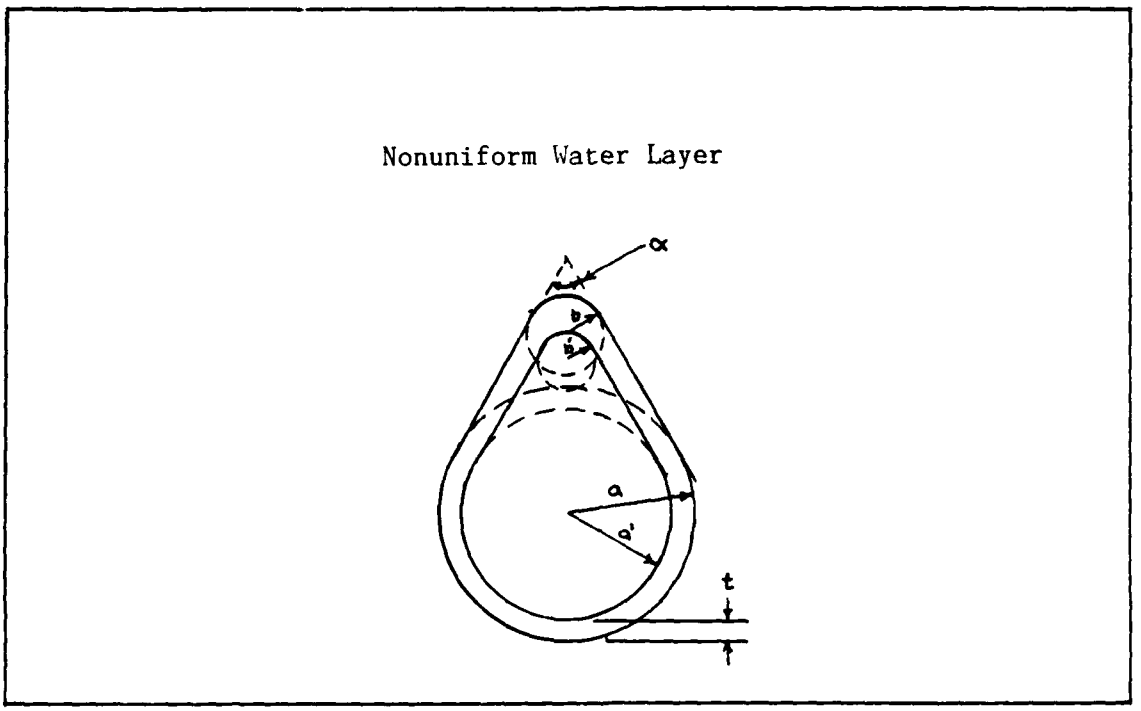

Figure 37. Sphere-Cone-Sphere Hailstone Model

ZDR was determined for various sizes of sphere-cone-spheroidal hailstone models and is shown in Figure 38. Equivolume spherical diameter is given by D = 2.07a and is varied from 2 through 26 mm. The hailstone models for Figure 38 have cone angle α = 60 degrees and radius ratio b/a = 0.5. The relative dielectric constant of the ice is the same as for the oblate spheroid.

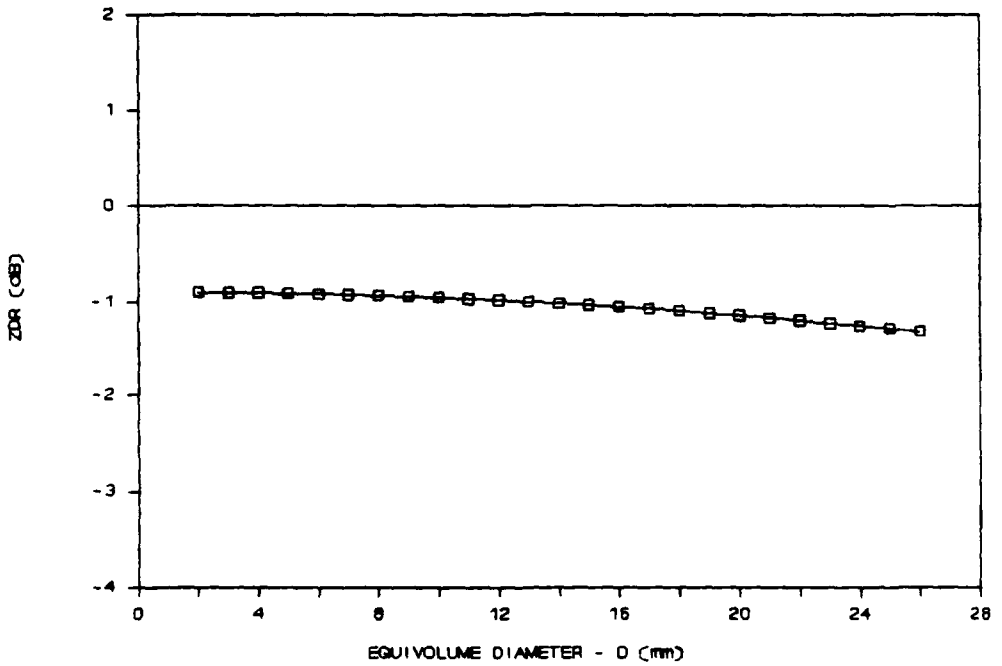

Figure 38. Z_{DR} vs. Equivolume Diameter for Sphere-Cone-Sphere

Sphere-Cone-Oblate Spheroid.

Figure 39 shows the sphere-cone-oblate spheroid hailstone model. Parameter c is the radius of the apex sphere. Parameters a and b are the oblate spheroid semiaxis lengths. Cone angle is given by angle α. Figure 40 shows Z_{DR} vs. equivolume spherical diameter (D). The following relationships hold for the hailstone models in Figure 40: c/a = 0.2, b/a = 0.5, α = 70 degrees, and D = 1.672a. The relative dielectric of the model is ϵ_r = 5.33 +j0.57.

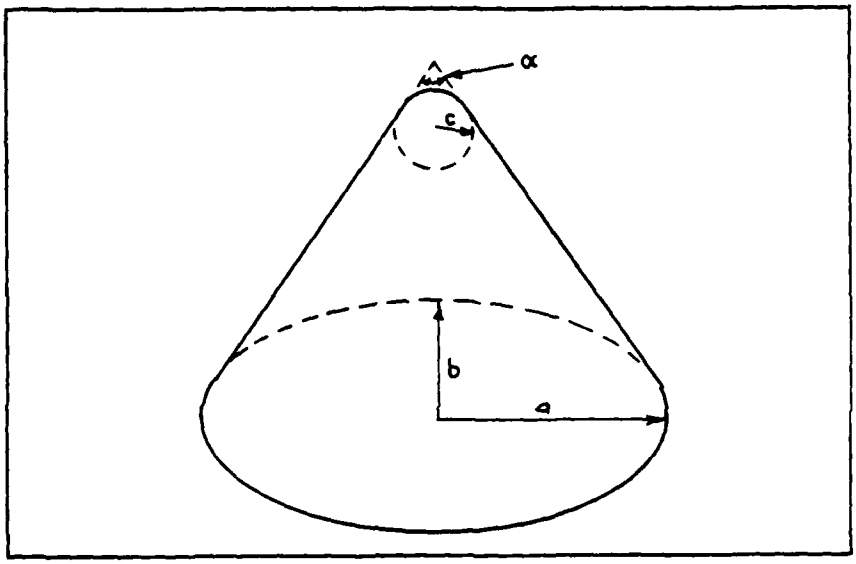

Figure 39. Sphere-Cone-Oblate Spheroid Hailstone Model

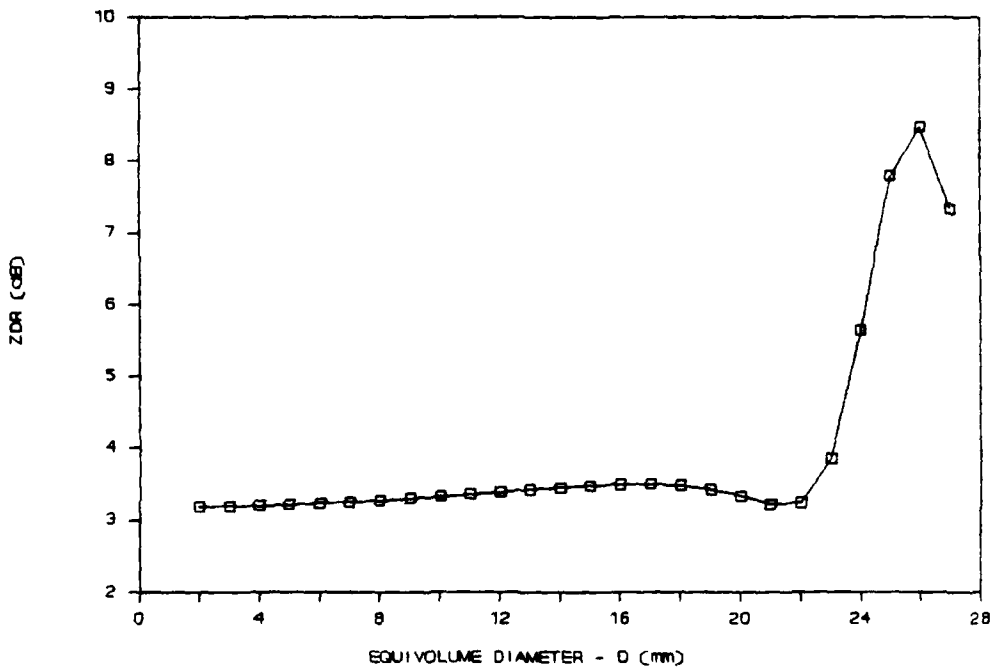

Figure 40. ZDR vs. Equivolume Diameter for Sphere-Cone-Oblate Spheroid

The scattering calculations for the hailstones in this appendix appeared to be exactly the same as those published by Aydin and Seliga (1:58-66).

Appendix B: EBCM FORTRAN Code Description

Introduction

This appendix briefly describes the three interactive FORTRAN programs used in this thesis. Major function, input, and output associated with each of the three programs are presented. MCON, MLAYRC, and MAINOR are the three programs discussed.

Figure 41 shows the coordinate system used. The incident wave propagates in the +z-direction and its polarization vector is specified by amplitude, A, and angle, ψ, from the x-axis in the xy-plane. Scatterer orientation is specified by angles Θ and ϕ where S is the axis of symmetry of the scatterer. The scattered field is evaluated in the xz-plane with 0 degrees in the forward or

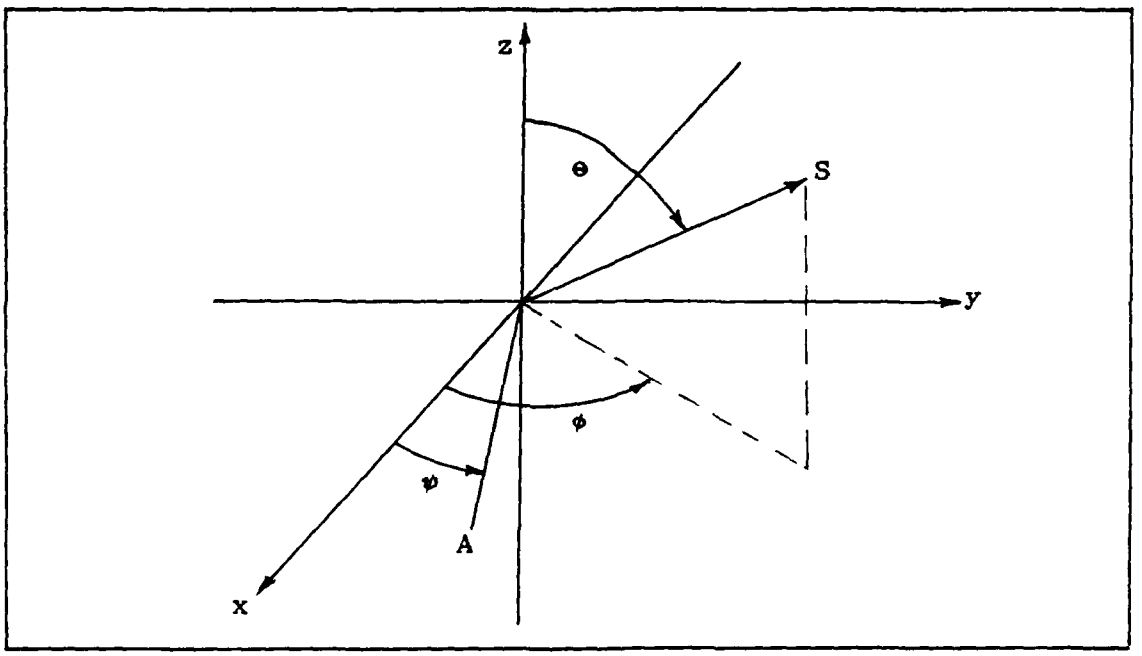

Figure 41. Coordinate System

+z-direction and 180 degrees in the backscattered or -z-direction. The scattering angle is equal to 90 degrees at the +x-axis.

MCON

MCON calculates the T-matrix for a nonlayered Wang hailstone model at the incident wave frequency of interest. Gaussian quadrature is used to perform the required numerical integration. Bessel functions are computed using downward recursion. Legendre functions are computed using upward recursion. Matrix inversions are accomplished using a Gauss-Jordan inversion technique.

Input. The interactive program prompts the user to enter the following variables:

A: Wang hailstone parameter (a) in cm

C: Wang hailstone parameter (c) in cm

LMDA: Wang hailstone parameter (λ)

WVLTH: Incident wavelength in cm

NRANK: Summation truncation value (N)

NTHETA: Number of nodes for Gaussian integration (multiple of 2)

IOUT: Convergence testing code (0 = NTHETA, 1 = NRANK, 2 = NM)

DCNR: Real part of hailstone dielectric constant

DCNI: Imaginary part of hailstone dielectric constant

Convergence Testing. The following procedure was carefully followed for variables NRANK, NTHETA, and IOUT.

1. Set NRANK = 10, NTHETA = 20, and IOUT = 0.

The program checks for convergence over NTHETA. Convergence occurs if the DSCS at ten scattering angles does not change by more than one percent as NTHETA increases to its specified value. If the program responds with

*** SOLUTION HAS CONVERGED ***

go to Step 2. If convergence is not achieved run the program again with NRANK = 10, IOUT = 0, and NTHETA increased by 2.

2. Set NRANK = 10, IOUT = 1 and NTHETA equal to its convergent value from Step 1. The program will run and check for convergence over NRANK. Convergence occurs if the DSCS at ten scattering angles does not change by more than one percent as NRANK increases to its specified value. If the program responds with

*** SOLUTION HAS CONVERGED ***

go to Step 3. If convergence is not achieved increase NRANK and run the program again with IOUT = 1 and NTHETA equal to its convergent value from Step 1.

3. Set NRANK and NTHETA equal to their convergent values and IOUT = 2. The program will run to convergence over NM. Variable NM corresponds to index m of the associated Legendre functions.

Output. The output of MCON consists of two data files: EBCM.DAT and T.DAT. EBCM.DAT contains the input variables used in computing the T-matrix. T.DAT contains the computed T-matrix.

MLAYRC

MLAYRC computes the T-matrix for a layered Wang hailstone model at the incident wave frequency of interest. Numerical techniques used in MLAYRC are the same as those used in MCON.

Input. The interactive program prompts the user to enter the same variables as in program MCON. Wang hailstone parameters a,c, and λ correspond to the external dimensions of the layered hailstone model. MLAYRC prompts the user to enter water layer thickness (t) and the real and imaginary parts of the dielectric constants for each layer of the hailstone model.

Convergence Testing. Convergence testing for MLAYRC is accomplished using the same procedure as in MCON.

Output. Same as for MCON.

MAINOR

MAINOR computes DSCS, scattering, absorption, and extinction cross sections for a specified incident wave and hailstone orientation. All scattering quantities are normalized to πc^2, where c is the Wang hailstone parameter.

Input. MAINOR uses the output files from MCON and MLAYRC to calculate the required scattering quantities. MAINOR also interactively prompts the user to enter the following variables:

AMPLAB: Amplitude (A from Figure 41) of incident wave

ANGLAB: Polarization angle (ψ from Figure 41) of incident wave

IOUT: 0 (no output file) or 1 (output file SCAT.DAT)

DLTANG: Scattering angle increment

NUANG: Number of scattering angles

NCASES: number of hailstone orientations

ANGINT: Hailstone orientation angle (θ from Figure 41)

ANGINP: Hailstone orientation angle (ϕ from Figure 41)

MAINOR will prompt the user for ANGINT and ANGINP for each desired hailstone orientation.

Output. Normalized DSCS (for each specified scattering angle), scattering, absorption, and extinction cross sections are displayed on the user's terminal screen. If requested, DSCS calculations are written to data file SCAT.DAT.

Bibliography

1. Aydin, K. and Seliga, T. A. "Differential Radar Scattering Properties of Modal Hail and Mixed-Phase Hydrometeors," Radio Science, 19: 58-66 (January-February 1984).

2. Barber, Peter W. "Resonance Electromagnetic Absorption by Nonspherical Dielectric Objects," IEEE Transactions on Microwave Theory and Techniques, MTT-25: 373-381 (May 1977).

3. Barber, Peter W. and Yeh, Cavour. "Scattering of Electromagnetic Waves by Arbitrarily Shaped Dielectric Bodies," Applied Optics, 14: 2864-2872 (December 1975).

4. Battan, L. J., Browning, S. R. and Herman, B. M. "Tables of the Radar Cross Sections of Dry and Wet Ice Spheres," Technical Report Number 21, Institute of Atmospheric Physics, University of Arizona, Tucson, June 1970.

5. Bringi, V. N. and Seliga, T. A. "Scattering from Axisymmetric Dielectrics or Perfect Conductors Imbedded in an Axisymmetric Dielectric," IEEE Transactions on Antennas and Propagation, AP-25: 575-580 (July 1977).

6. Kishk, A. A. and Shafai, L. "Numerical Solution of Scattering from Coated Bodies of Revolution using Different Integral Equation Formulations," IEE Proceedings, 133: 227-232 (June 1986).

7. Knott, Eugene F. and others. Radar Cross Section. Norwood MA: Artech House, 1985.

8. Medgyesi-Mitschang, L. N. and Eftimiu, C. "Scattering from Axisymmetric Obstacles Embedded in Axisymmetric Dielectrics: The Method of Moments Solution," Applied Physics, 19: 275-285 (July 1979).

9. Morgan, Michael A. and Mei, Kenneth K. "Finite-Element Computation of Scattering by Inhomogeneous Penetrable Bodies of Revolution," IEEE Transactions on Antennas and Propagation, AP-27: 202-214 (March 1979).

10. Morse, Philip M. and Feshbach. Methods of Theoretical Physics. New York: McGraw-Hill, 1953.

11. Peterson, B. and Strom, S. "T-Matrix Formulation of Electromagnetic Scattering from Multilayered Scatterers," Physical Review D, 10: 2670-2684 (15 October 1974).

12. Ray, Peter S. "Broadband Complex Refractive Indices of Ice and Water," Applied Optics, 11: 1836-1844 (August 1972).

13. Stratton, Julius A. Electromagnetic Theory. New York: McGraw-Hill, 1941.

14. Stutzman, Warren L. A Review of Theoretical Modeling of Millimeter Wave Propagation through Precipitation. Electrical Engineering Department, Virginia Polytechnic Institute and State University, Blacksburg VA, May 1980.

15. Wang, Dau-Sing and Barber, Peter W. "Scattering by Inhomogeneous Nonspherical Objects," Applied Optics, 18: 1190-1197 (15 April 1979).

16. Wang, Pao K., Greenwald, Thomas J. and Wang, Jianlu. "A Three Parameter Representation of the Shape and Size Distributions of Hailstones - A Case Study," Journal of the Atmospheric Sciences, 44: 1062-1070 (April 1987).

17. Warner, C. and Hizal, A. Scattering and Depolarization by Spheroidal Raindrops," Radio Science, 11: 921-930 (November 1976).

18. Waterman, P. C. "Matrix Formulation of Electromagnetic Scattering," Proceedings of the IEEE, 53: 805-812 (August 1965).

19. -----. "Symmetry, Unitarity, and Geometry in Electromagnetic Scattering," Physical Review D, 3: 825-839 (15 February 1971).

VITA

Captain Brian J. Stutz [redacted] He graduated from high school in Apple Creek, Ohio, in 1980 and attended Ohio Northern University in Ada, Ohio. On 23 May 1983 he enlisted in the USAF through the College Senior Engineer Program. He graduated from Ohio Northern University with the degree of Bachelor of Science in Electrical Engineering in May 1984. After graduation, he attended the Air Force Officer Training School in San Antonio, Texas, and was commissioned a Second Lieutenant in the USAF in August 1984. He was assigned to the Electronic Security Command at Kelly AFB, Texas where he served as Test Director until entering the School of Engineering, Air Force Institute of Technology, in June 1987.

[redacted]

REPORT DOCUMENTATION PAGE

Form Approved OMB No. 0704-0188

1a. REPORT SECURITY CLASSIFICATION: UNCLASSIFIED	1b. RESTRICTIVE MARKINGS
2a. SECURITY CLASSIFICATION AUTHORITY	3. DISTRIBUTION/AVAILABILITY OF REPORT: Approved for public release; distribution unlimited
2b. DECLASSIFICATION/DOWNGRADING SCHEDULE	
4. PERFORMING ORGANIZATION REPORT NUMBER(S): AFIT/GE/ENG/88D-51	5. MONITORING ORGANIZATION REPORT NUMBER(S)
6a. NAME OF PERFORMING ORGANIZATION: School of Engineering; 6b. OFFICE SYMBOL (If applicable): AFIT/ENG	7a. NAME OF MONITORING ORGANIZATION
6c. ADDRESS (City, State, and ZIP Code): Air Force Institute of Technology, Wright-Patterson AFB OH 45433-6583	7b. ADDRESS (City, State, and ZIP Code)
8a. NAME OF FUNDING/SPONSORING ORGANIZATION: AF Wright Aeronautical Lab.; 8b. OFFICE SYMBOL (If applicable): AFWAL/CDJA	9. PROCUREMENT INSTRUMENT IDENTIFICATION NUMBER
8c. ADDRESS (City, State, and ZIP Code): AFWAL/CDJA, Wright-Patterson AFB OH 45433	10. SOURCE OF FUNDING NUMBERS: PROGRAM ELEMENT NO. / PROJECT NO. / TASK NO / WORK UNIT ACCESSION NO.

11. TITLE (Include Security Classification): See Box 19

12. PERSONAL AUTHOR(S): Brian J. Stutz, Capt, USAF

13a. TYPE OF REPORT	13b. TIME COVERED	14. DATE OF REPORT (Year, Month, Day)	15. PAGE COUNT
MS Thesis	FROM _____ TO _____	1988 December	82

16. SUPPLEMENTARY NOTATION

17. COSATI CODES			18. SUBJECT TERMS (Continue on reverse if necessary and identify by block number)
FIELD	GROUP	SUB-GROUP	
20	08		Electromagnetic Scattering, Scattering, Hydrometeors
04	02		Atmospheric Precipitation

19. ABSTRACT (Continue on reverse if necessary and identify by block number)

Title: SCATTERING CALCULATIONS FOR VARIOUS HAILSTONE MODELS USING THE EXTENDED BOUNDARY CONDITION METHOD

Thesis Advisor: Harry Barksdale, Major, USAF
Assistant Professor of Electrical Engineering

Abstract: See reverse side.

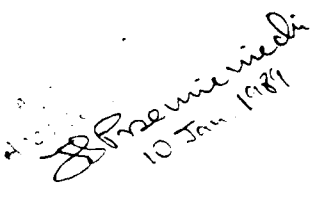

20. DISTRIBUTION/AVAILABILITY OF ABSTRACT: ☒ UNCLASSIFIED/UNLIMITED ☐ SAME AS RPT. ☐ DTIC USERS	21. ABSTRACT SECURITY CLASSIFICATION: UNCLASSIFIED
22a. NAME OF RESPONSIBLE INDIVIDUAL: Harry Barksdale, Major, USAF	22b. TELEPHONE (Include Area Code): 513-255-2549 / 22c. OFFICE SYMBOL: AFIT/ENG

DD Form 1473, JUN 86 — Previous editions are obsolete. — SECURITY CLASSIFICATION OF THIS PAGE

Block 19 continued:

Abstract

The extended boundary condition method is applied to 3-D electromagnetic scattering problems involving hailstones modeled using Wang's three parameter hailstone representation. The theory of the extended boundary condition method is presented for various layered and nonlayered hailstone models for incident wavelengths of 1 and 10 cm. The layered hailstone models are constructed of ice surrounded by a layer of water and represent melting hailstones. Nonlayered hailstone models represent nonmelting hailstones and are composed entirely of ice. Hailstone size, shape, and structure were varied to determine their effect on scattering and absorption characteristics. The results indicate that resonance scattering is very sensitive to hailstone size, shape, and structure. Rayleigh scattering is sensitive to size and structure but much less dependent on hailstone shape.